An in vitro assay for entry into cilia reveals unique properties of the soluble diffusion barrier

David K. Breslow,[1] Elena F. Koslover,[2] Federica Seydel,[1] Andrew J. Spakowitz,[2] and Maxence V. Nachury[1]

[1]Department of Molecular and Cellular Physiology and [2]Department of Chemical Engineering, Stanford University School of Medicine, Stanford, CA 94305

Specific proteins are concentrated within primary cilia, whereas others remain excluded. To understand the mechanistic basis of entry into cilia, we developed an in vitro assay using cells in which the plasma membrane was permeabilized, but the ciliary membrane was left intact. Using a diffusion-to-capture system and quantitative analysis, we find that proteins >9 nm in diameter (~100 kD) are restricted from entering cilia, and we confirm these findings in vivo. Interference with the nuclear pore complex (NPC) or the actin cytoskeleton in permeabilized cells demonstrated that the ciliary diffusion barrier is mechanistically distinct from those of the NPC or the axon initial segment. Moreover, applying a mass transport model to this system revealed diffusion coefficients for soluble and membrane proteins within cilia that are compatible with rapid exploration of the ciliary space in the absence of active transport. Our results indicate that large proteins require active transport for entry into cilia but not necessarily for movement inside cilia.

Introduction

The primary cilium organizes a variety of signaling cascades (G protein–coupled receptors [GPCRs], Hedgehog, and others) by dynamically concentrating signaling components (Goetz and Anderson, 2010; Nachury et al., 2010). A major unanswered question is how cilia concentrate signaling proteins despite topological continuities between plasma membrane and ciliary membrane and between cytosol and ciliary lumen. In the case of membrane proteins, lateral exchange between plasma and ciliary membranes is prevented by a septin-based diffusion barrier at the transition zone, a region at the base of cilia (Hu et al., 2010; Chih et al., 2012; Reiter et al., 2012), and by tethering of some plasma membrane proteins to the actin cytoskeleton (Francis et al., 2011). Conversely, it remains unclear whether a ciliary diffusion barrier exists for soluble proteins and, were it to exist, how it might operate.

On one hand, Kee et al. (2012) proposed that a size-dependent diffusion barrier restricts entry of cytosolic proteins into cilia. Specifically, after microinjection into the cytosol, fluorescent probes larger than ~40 kD were not detectable in cilia. This study also suggested that nucleoporins (Nups) localize near the base of the cilium to restrict protein entry. On the other hand, Calvert et al. (2010; Najafi et al., 2012) have found no evidence for a diffusion barrier at the connecting cilium of rod photoreceptors, a structure analogous to the transition zone of primary cilia. First, the kinetics and energy independence of arrestin (47 kD) and transducin (27 kD) translocation through the connecting cilium are fully accounted for by free diffusion (Nair et al., 2005; Rosenzweig et al., 2007). Second, proteins 27–81 kD in size were found to cross the connecting cilium at the same rate (Najafi et al., 2012). Yet, at steady state, the larger proteins do not distribute evenly between inner and outer segments (equivalents of the cell body and the distal part of the cilium, respectively). Instead, the tight packing of disk membranes in the outer segment limits the volume accessible to large proteins, and these steric effects result in an apparent decrease in protein concentration in the outer segment. The absence of flux measurements by Kee et al. (2012) and their inability to resolve the base of cilia raise the possibility that steric effects may account for the observed size-dependent distribution of probes in primary cilia versus cytoplasm (Najafi and Calvert, 2012).

Here, we establish and validate a permeabilized cell assay to directly and quantitatively test whether soluble protein entry into mammalian primary cilia is gated by a diffusion barrier. Using this system, we find that primary cilia possess a size-dependent

Correspondence to Maxence V. Nachury: nachury@stanford.edu

Abbreviations used in this paper: FRB, FKBP12-rapamycin binding domain; FKBP, FK506-binding protein; GBP, GFP-binding protein; GPCR, G protein–coupled receptor; IFT, intraflagellar transport; Luc, luciferase; MBP, maltose-binding protein; MM, molecular mass; NPC, nuclear pore complex; Nup, nucleoporin; PFO, perfringolysin O; Sstr3, somatostatin receptor 3; TIRF, total internal reflection fluorescence; Trx, thioredoxin.

The Rockefeller University Press $30.00
J. Cell Biol. Vol. 203 No. 1 129–147
www.jcb.org/cgi/doi/10.1083/jcb.201212024

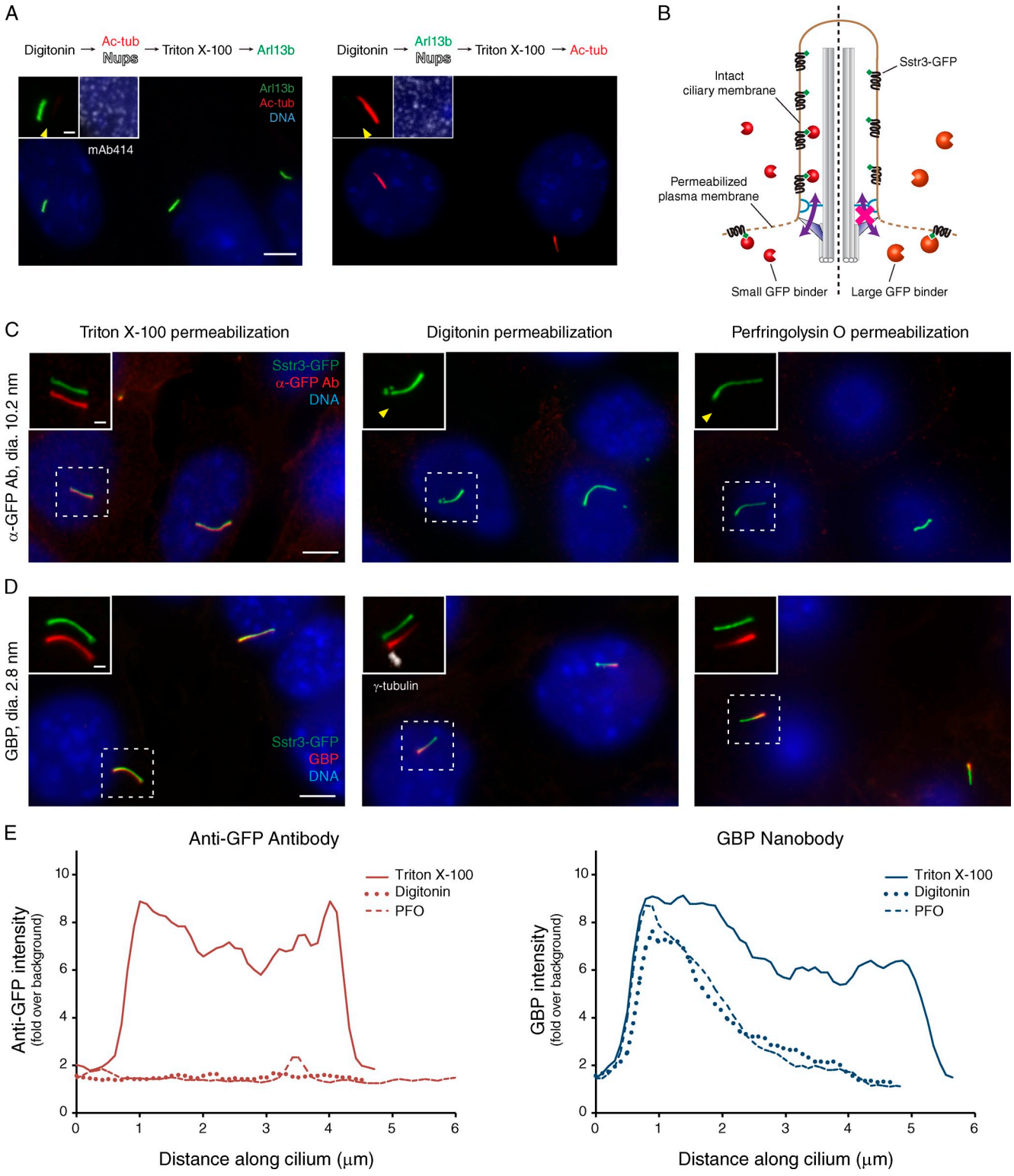

Figure 1. **Ciliary proteins are not accessible to antibodies in digitonin-permeabilized cells.** (A) IMCD3 cells were fixed, permeabilized with 30 μg/ml digitonin, and incubated for 10 min with antibodies to ciliary proteins and to nucleoporins (Nups). After removal of unbound antibodies, cells were permeabilized with Triton X-100 and stained with additional antibodies. Left insets show primary cilia with channels shifted to aid visualization. Arrowheads point to the cilium base in the acetylated tubulin channel (left) or the Arl13b channel (right). Right insets show staining of Nups and DNA. Ac-tub, acylated tubulin. (B) Overview of assay for soluble protein entry into primary cilia. IMCD3 cells are first treated with digitonin or PFO, which permeabilizes the plasma membrane while leaving the ciliary membrane intact. An exogenously added small GBP can cross from the cytoplasmic compartment into the cilium (left), where it is captured by GFP fused to the intracellular tail of the ciliary GPCR Sstr3. (right) A large GBP (e.g., an antibody) cannot enter the cilium and only accesses the pool of Sstr3-GFP present in the plasma membrane. (C) IMCD3 cells expressing Sstr3-GFP were stained with an anti-GFP antibody following a conventional immunofluorescence protocol using Triton X-100 for permeabilization (left) or in live cells permeabilized with digitonin (middle) or PFO (right). Insets show primary cilia with GFP and anti-GFP channels shifted to aid visualization. Arrowheads point to the base of the cilium in the GBP channel.

diffusion barrier that is mechanistically distinct from those found at the axon initial segment and the nuclear pore complex (NPC). We anticipate that our assay will be a powerful tool for mechanistic studies of trafficking to cilia and provide a basis for understanding how cilia regulate signal transduction.

Results

A permeabilized cell system for ciliary trafficking

In the course of observations on the lipid composition of primary cilia, we found that very low amounts of the cholesterol-dependent detergent digitonin selectively permeabilize the plasma membrane while leaving the ciliary membrane intact. This selective permeabilization is illustrated by the failure of antibodies against ciliary markers (e.g., acetylated α-tubulin and Arl13b) to stain primary cilia in digitonin-permeabilized cells despite strongly labeling cilia after permeabilization with 0.1% Triton X-100 (Fig. 1 A). In contrast, cytoplasmically exposed Nups at the nuclear envelope are readily detected by the mAb414 antibody after permeabilization with digitonin. Our results therefore suggest that after digitonin permeabilization, (a) the ciliary membrane remains intact, and (b) antibodies are not able to enter cilia from the cytosol.

To verify and extend these results, we stably expressed the somatostatin receptor 3 (Sstr3), a GPCR that is targeted to primary cilia, in IMCD3–Flp-In cells. For visualization, Sstr3 was tagged on its intracellular tail with GFP and the S tag. These cells were permeabilized with digitonin, incubated on ice with antibodies against GFP or the S tag, and then fixed and stained. Using this assay, we found that both anti-GFP and anti–S tag antibodies fail to access ciliary Sstr3-S-GFP after digitonin permeabilization but give strong ciliary staining in a conventional, Triton X-100–based immunofluorescence protocol (Figs. 1, B and C; and S1 B). For both antibodies, the plasma membrane pool of Sstr3-S-GFP is accessible in digitonin-permeabilized cells, thus confirming plasma membrane permeabilization and successful immunological detection of Sstr3-S-GFP under our experimental conditions (Fig. S1, A and B). Similar results were obtained when cells were permeabilized with the cholesterol-dependent pore-forming toxin perfringolysin O (PFO; Figs. 1 C and S1 A).

We next tested whether the size of the GFP binder affects its ability to enter primary cilia of digitonin-permeabilized cells. Here, we took advantage of a miniaturized GFP-binding protein (GBP; Kirchhofer et al., 2010). In contrast to the anti-GFP antibody, the 13.5-kD GBP readily gained access to ciliary Sstr3-GFP in digitonin or PFO-permeabilized cells (Fig. 1 D). A similar size-dependent entry of GBPs is observed when GFP is displayed inside cilia via fusion to the ciliary targeting signal of Pkhd1 ($Pkhd1^{ICD}$; Fig. S1 C; Follit et al., 2010). Notably, a gradient of GBP signal from the base to the tip of the cilium was often seen in digitonin-permeabilized cells, consistent with GBP entering at the base of the cilium from the cytoplasmic compartment (Fig. 1, B, D, and E). This gradient of signal is not seen in GBP-stained cells after Triton X-100 permeabilization (Fig. 1, D and E), indicating that GBP entry at the base of cilia is specific to digitonin-permeabilized cells.

Permeabilization with PFO consistently yields the same results as digitonin, even though PFO is a pore-forming oligomeric cytolysin, whereas digitonin is a chemical detergent (Heuck et al., 2010). PFO-induced pores have a stereotypical diameter of ∼30 nm (Olofsson et al., 1993; Czajkowsky et al., 2004), whereas the diameter of an antibody is 10 nm, thus ruling out the possibility that PFO pore size accounts for size-dependent entry into cilia. Finally, two independent kinetic experiments (see Figs. 3 C and 8 C) confirm that GBPs entering cilia first appear in proximal regions near the base of the cilium before gaining access to more distal receptors. Collectively, the aforementioned observations confirm that digitonin and PFO selectively permeabilize the plasma membrane while leaving the ciliary membrane intact.

We further validated our permeabilized cell system by assaying two key features of primary cilia. First, FRAP of ciliary Sstr3-GFP in permeabilized cells confirms that the membrane diffusion barrier seen in live cells (Hu et al., 2010) remains functional, as unbleached receptors in the plasma membrane cannot move into the cilium within 5 min of bleaching (Fig. 2 A). As a control, we note that Sstr3 moves freely within the ciliary membrane, as assessed by half-cilium FRAP, and within the plasma membrane, as evidenced by rapid fluorescence recovery in bleached regions of the plasma membrane near the cilium (Fig. 2 A; Ye et al., 2013).

Second, we investigated intraflagellar transport (IFT), the motor-driven movement of clusters of IFT complexes along the axoneme (Pedersen and Rosenbaum, 2008). Live imaging of GFP-tagged IFT88 (an IFT-B complex subunit) revealed that IFT stops in permeabilized cells (Fig. 2 B and Ye et al., 2013). Because ATP is lost from permeabilized cells (Ye et al., 2013) and cytoplasmic factors may similarly be washed away, we reasoned that it should be possible to reactivate IFT by adding cellular extracts and energy as long as ciliary structures have not been profoundly altered by digitonin permeabilization. Using extracts from bovine retina, a rich source of ciliary transport factors (Jin et al., 2010), or from *Xenopus laevis* eggs, we observed a resumption of GFP-IFT88 movement inside nearly all tested cilia (Fig. 2 B). These results strongly suggest that cilia from permeabilized cells are functionally intact.

Several mechanisms may act in concert to account for the selective permeabilization of the plasma membrane. First, both PFO and digitonin interact with cholesterol and require cholesterol for permeabilization (Schulz, 1990; Flanagan et al., 2009). Thus, a lower amount of cholesterol in the ciliary membrane

Ab, antibody; dia., diameter. (D) Cells expressing Sstr3-GFP were stained with GBP labeled with Alexa Fluor 647 as in C. Insets show primary cilia with channels shifted. PFO- and digitonin-treated cells exhibit a gradient of GBP signal from cilium base (marked by γ-tubulin in white) to tip. (E) Line graphs of ciliary signals of GFP binders reveal that the base-to-tip gradient of GBP distribution is specific to semipermeabilized cells and that the anti-GFP antibody is absent from semipermeabilized cells. Lines were drawn through cilia from images in C and D, and intensity relative to background was measured with ImageJ. The data shown are from a representative cell, with >10 cells analyzed in each of four experiments. Bars: (main images) 5 µm; (insets) 1 µm.

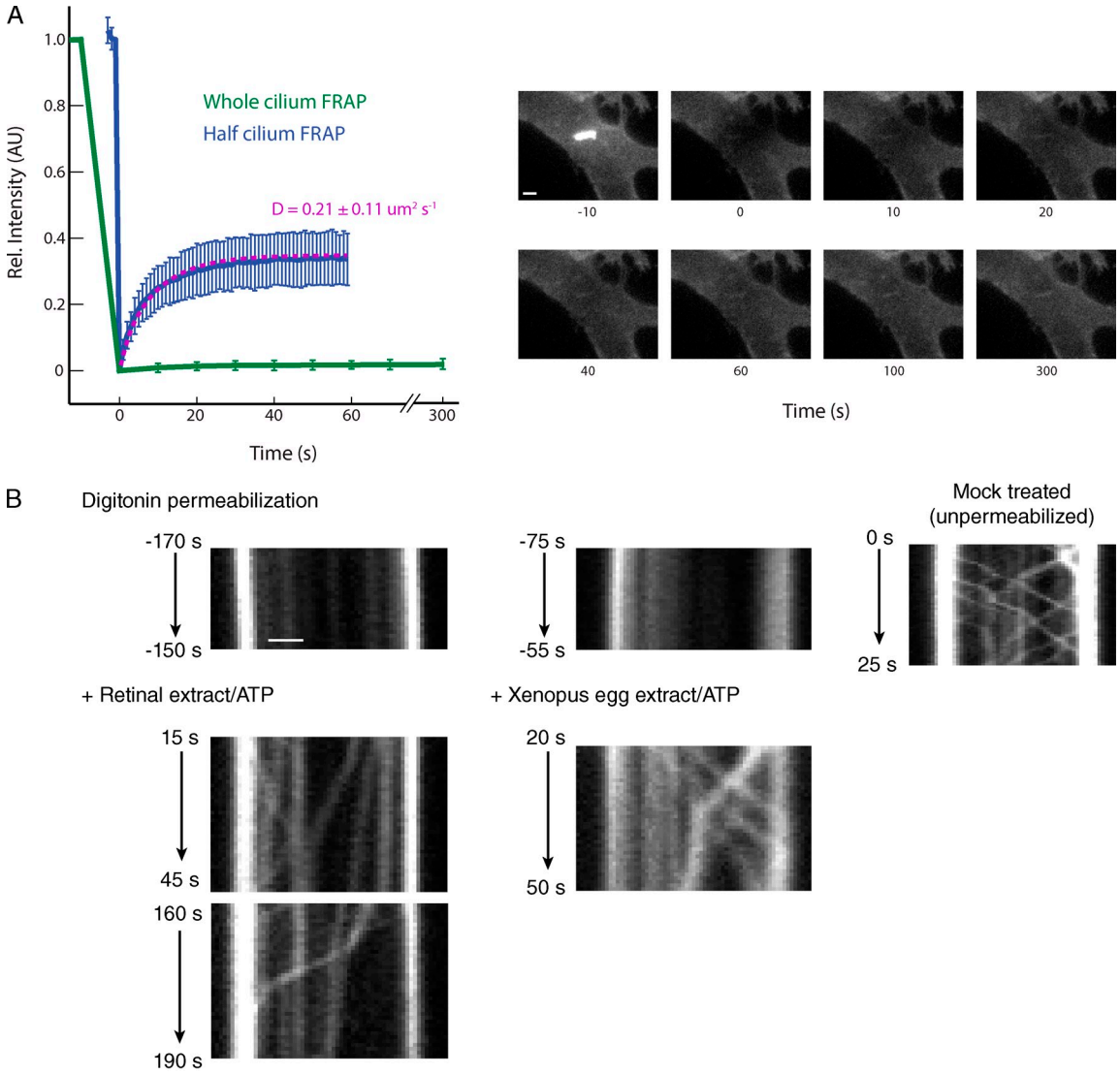

Figure 2. **Cilia from digitonin-permeabilized cells are functionally intact.** (A) The integrity of the membrane diffusion barrier at the base of cilia was assessed by whole-cilium FRAP. Photobleaching of the distal half of the cilium was performed to test Sstr3 mobility with the ciliary membrane. Averaged fluorescence recovery traces for the bleached region are plotted on the left ($n \geq 14$; error bars indicate standard deviation). The Sstr3-GFP diffusion coefficient was determined by fitting observed half-cilium recovery traces to an expected curve (see Materials and methods) and was used to calculate the recovery curve shown in purple. Images on the right show representative data for whole-cilium FRAP. Rel., relative; AU, arbitrary unit. Bar, 2 µm. (B) Reconstitution of IFT in digitonin-permeabilized cells. Kymographs of GFP-IFT88 movement reveal that IFT trains do not move in digitonin-permeabilized cells. Addition of an ATP regenerating system and extracts from bovine retina (left) or *Xenopus* eggs (middle) reactivates IFT movement in anterograde and retrograde directions. IFT movement in a mock-permeabilized (intact) cell is shown on the right. Bar, 1 µm.

or a reduced accessibility of cholesterol (e.g., caused by association with lipid raft domains) may prevent permeabilization of the ciliary membrane. Similarly, low cholesterol levels in the nuclear envelope enabled the use of digitonin for nuclear transport assays (Adam et al., 1990). Using filipin to assess cholesterol levels in primary cilia of IMCD3 cells, we found no enrichment of cholesterol in ciliary versus plasma membrane (Fig. S2 A). Second, primary cilia may avoid permeabilization by low amounts of digitonin because of reduced accessibility to added buffer. The majority of cilia were found on the ventral surface of cells under our experimental conditions, as indicated by total internal reflection fluorescence (TIRF) microscopy (Fig. S2 B). Third, it is possible that cilia remain intact because limiting amounts of digitonin are more likely to permeabilize the much larger portion of the cell surface corresponding to the plasma membrane than the comparatively small fraction (~1%) represented by a single cilium. Indeed, given that a small fraction of cells typically remain unpermeabilized after digitonin treatment, the probability of disrupting the ciliary membrane may be quite low.

Quantitative analysis of the ciliary diffusion barrier

To determine the size cutoff for passive entry into primary cilia, we generated a panel of six GBP fusions with proteins of increasing sizes and measured their hydrodynamic diameters by size exclusion chromatography (Fig. 3 B). Incubation of digitonin-permeabilized cells with dye-labeled GBP fusions revealed a

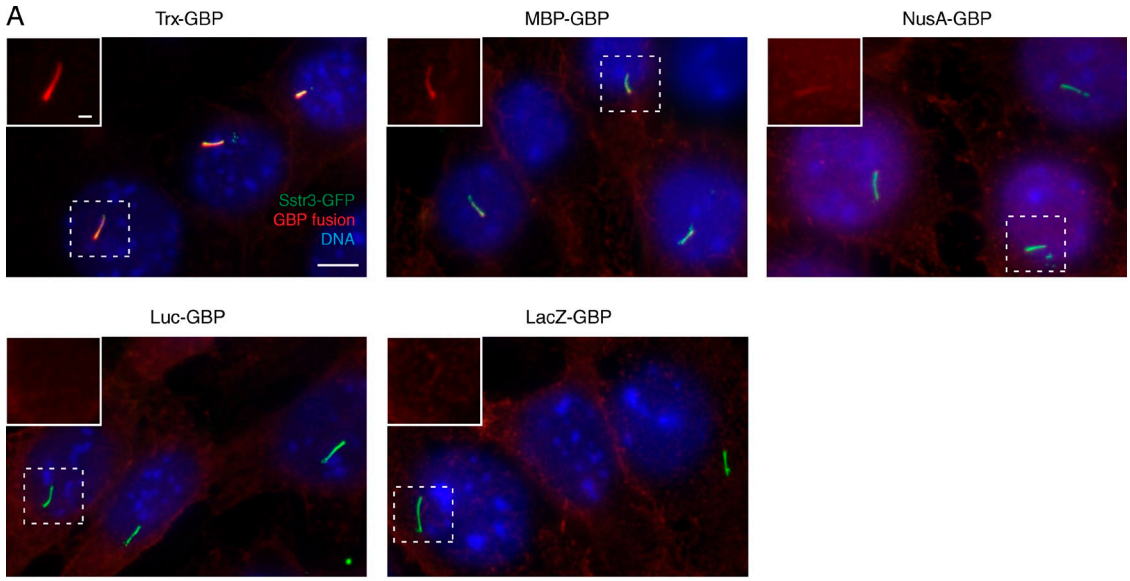

B

GFP Binder	MM (kD)	Stokes Radius (nm)	Ciliary Entry
GBP Nanobody	13.5	1.4	++++
Thioredoxin-GBP	26	2.4	++++
MBP-GBP	57	3.1	++
ZZ-GBP	29	3.6	+
NusA-GBP	70	4.3	+/-
Luciferase-GBP	75	4.3	-
Anti-GFP Ab	145	5.1	-
ZZ-GBP + IgG	175	>5.1	-
LacZ-GBP	520	6.1	-

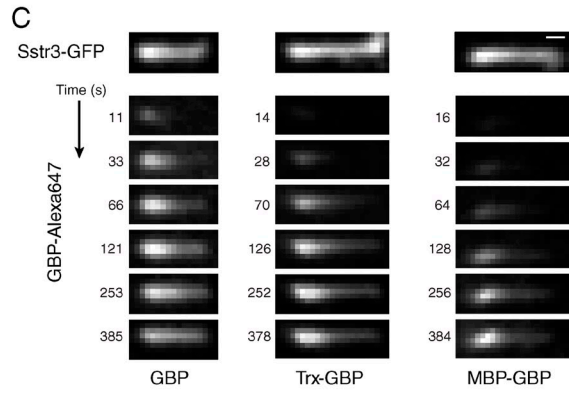

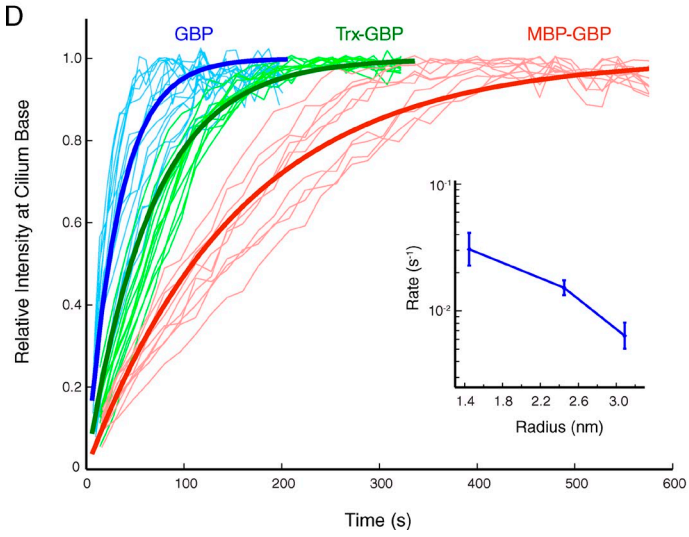

Figure 3. **A series of GBP fusions reveals the size limit of the ciliary diffusion barrier.** (A) Digitonin-permeabilized cells were incubated at room temperature for 10 min with the indicated dye-labeled GBP fusion proteins. Insets show cilia in GBP channel only. Trx, thioredoxin; MBP, maltose-binding protein; NusA, N-using substance A; Luc, firefly luciferase; LacZ, β-galactosidase. Bars: (main images) 5 µm; (insets) 1 µm. (B) Properties of GBPs including molecular mass (MM), Stokes radius, and degree of ciliary entry in digitonin-permeabilized IMCD3 cells expressing Sstr3-GFP. The relative degree of entry seen in A is denoted by the number of + symbols or by a − symbol in cases where no entry was detected. ZZ, tandem Z domain from *S. aureus* protein A; IgG, immunoglobulin G. (C) Kinetic analysis of GBP entry into cilia of permeabilized IMCD3 cells. GBP alone, Trx-GBP, and MBP-GBP were added at 110 nM, and capture by ciliary Sstr3-GFP was monitored by confocal microscopy. Bar, 1 µm. (D) The GBP signal at the most proximal region of the cilium is plotted versus time for GBP alone, Trx-GBP, and MBP-GBP. Traces for individual cilia are shown in thin lines ($n \geq 10$). Fitted exponential curves corresponding to the mean entry rate are shown in thick lines. Inset graph at right shows fitted rate constants (plotted on a logarithmic scale) versus measured Stokes radius. Error bars indicate standard deviations.

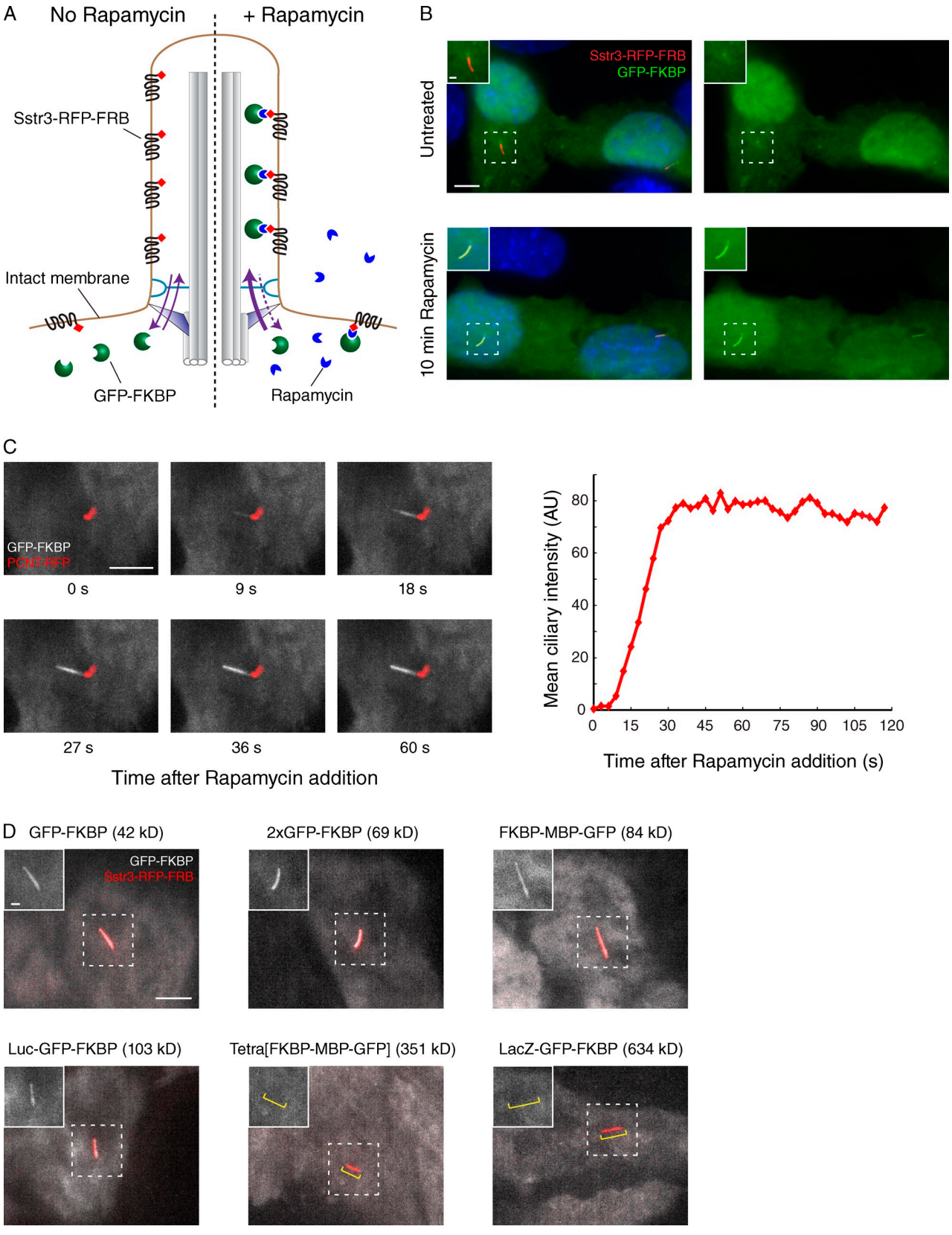

Figure 4. **Inducible diffusion to capture in live cells confirms the existence of a ciliary diffusion barrier.** (A) Schematic of the in vivo diffusion to capture assay based on rapamycin-inducible binding of FRB and FKBP domains. Cells expressing Sstr3-RFP-FRB in cilia were transfected with plasmids encoding FKBP- and GFP-bearing fusion proteins. In the absence of rapamycin (left), GFP-FKBP fusions are found in the cytoplasm; after rapamycin addition (right), irreversible dimerization of FRB with FKBP leads to the capture of any GFP-FKBP that diffuses into cilia. (B) Cells were fixed and imaged before and after rapamycin-induced accumulation of GFP-FKBP inside cilia. Insets show enlarged views of cilia. A weak enrichment of GFP-FKBP around the base of cilia is caused by a nonspecific affinity of GFP for pericentriolar material (Fig. S4 B). (C) Pericentrin (PCNT) was cotransfected with GFP-FKBP to mark the base

progressive decrease in ciliary entry for proteins above 4.8 nm in diameter and no detectable ciliary signal for proteins above ∼8.6 nm in diameter (Fig. 3, A and B). The larger GBP fusions have the ability to bind Sstr3-GFP because all GBPs stain plasma membrane–localized Sstr3-GFP in digitonin-permeabilized cells (Fig. 3 A) and detect ciliary Sstr3-GFP in cells permeabilized with Triton X-100 (Fig. S3 A). To further test whether size is the primary factor governing ciliary entry, we generated a GBP fusion containing two copies of the IgG-binding Z domain derived from *Staphylococcus aureus* protein A (Nilsson et al., 1987). The ZZ-GBP fusion alone enters cilia of digitonin-permeabilized cells, but preincubation with rabbit IgG renders the enlarged ZZ-GBP:IgG unable to enter cilia (Fig. S3 B).

We next determined how GBP size affects the rate of entry using live confocal microscopy. As expected, the GBP signal inside cilia appears first at the base, before increasing in intensity and spreading distally toward the tip (Fig. 3 C and Video 1). To determine entry rates, we measured the time-dependent increase of the GBP signal inside cilia; only the signal at the most proximal segment of the cilium was analyzed to isolate entry from diffusional movement of GBPs within the cilium. The resulting data fit a first-order exponential equation, and the fitted entry rate decreases sharply with increasing GBP size (Fig. 3 D). These results echo those obtained in a previous study on rates of diffusion through the NPC (Mohr et al., 2009) and firmly establish that a size-dependent permeability barrier controls protein entry into cilia.

In vivo validation of the permeability barrier

To confirm that the basic properties of the permeability barrier are preserved in semipermeabilized cells, we sought to better characterize the permeability barrier in intact cells. Here, we leveraged a well-characterized system for chemical induction of heterodimerization that consists of the protein moieties FK506-binding protein (FKBP) and FKBP12-rapamycin binding domain (FRB) and the small molecule rapamycin (Komatsu et al., 2010). FRB was fused to Sstr3 together with the fluorescent protein TagRFP-T, and GFP was fused to FKBP (Fig. 4 A). In untreated cells, Sstr3-RFP-FRB is concentrated within the ciliary membrane, whereas GFP-FKBP is diffusely cytoplasmic (Fig. 4 B). We note a slight enrichment of GFP-FKBP near the basal body, in agreement with our observation that GFP alone is slightly enriched at the centrosome (Fig. S4 B). Upon addition of rapamycin, GFP-FKBP accumulated in cilia (Fig. 4 B), confirming that a small protein (molecular mass [MM] = 42 kD) rapidly diffuses into cilia. The accumulation of GFP-FKBP into cilia proceeded with very rapid kinetics, with the intensity of GFP-FKBP inside cilia plateauing within 45 s of rapamycin addition (Fig. 4 C). To assess whether a ciliary permeability barrier exists in intact cells, we fused GFP-FKBP to proteins of increasing size and found that the tetrameric fusions Tetra[FKBP–maltose-binding protein (MBP)-GFP] (MM = 351 kD) and LacZ-GFP-FKBP (MM = 634 kD) are excluded from cilia within our experimental time frame (Fig. 4 D). Importantly, these constructs are functional, as they can be rapidly recruited to the plasma membrane by Lyn-FRB (Fig. S3 D). We limited our analysis to <10 min, as FRAP analysis shows that the ciliary levels of Sstr3 start to increase 10 min after photobleaching, most likely because of the trafficking of newly synthesized Sstr3 to cilia. Meanwhile, the fusions 2×GFP-FKBP (69 kD), MBP-GFP-FKBP (84 kD), and luciferase (Luc)-GFP-FKBP (103 kD) were able to enter cilia within 6 min of rapamycin addition.

Although the molecular weight limit we observed in vivo is slightly greater than the value we found in vitro, the actual differences in hydrodynamic radii between Luc-GFP-FKBP (Stokes radius = 4.4 nm; Lin et al., 2013) and Luc-GBP (Stokes radius = 4.3 nm) are minimal. Furthermore, we surmised that transient transfection of GFP-FKBP fusions generates considerably higher protein concentrations than used in our in vitro system (55 nM) and that such a high concentration of the diffusion probe sufficiently increases the flux into cilia to generate a detectable signal. Consistent with this interpretation, low signals of Luc-GBP can be detected within cilia of semipermeabilized cells when the Luc-GBP concentration is increased sixfold and incubation time is increased fourfold (Fig. S3 C). Together with the IFT reactivation results, our in vivo system shows that the basic properties of primary cilia are conserved between live cells and permeabilized cells.

Unique properties of the ciliary diffusion barrier

Leveraging the ease of manipulation afforded by an in vitro system, we sought to characterize the molecular properties of the ciliary permeability barrier. At the axon initial segment, a barrier of densely cross-linked filaments separates the cell body from the axonal compartment (Winckler et al., 1999; Nakada et al., 2003; Song et al., 2009). Although the axonal permeability is disrupted by the actin poison Cytochalasin D (Song et al., 2009), treatment of IMCD3 cells with Cytochalasin D for 30 min before digitonin permeabilization did not permit ciliary entry of any GBPs larger than the size cutoff defined in Fig. 3 (Fig. 5 A).

Next, we examined the relationship between the ciliary diffusion barrier and the NPC barrier, which is formed by a hydrophobic hydrogel of FG repeats. Elements of the nuclear transport machinery have been implicated in ciliary trafficking, and it was recently proposed that Nups prevent passive protein entry into cilia (Dishinger et al., 2010; Fan et al., 2011; Kee et al., 2012). We tested the possibility that Nups restrict ciliary entry by applying reagents that modulate the NPC hydrogel to our assay. First, we examined 1,2-trans-cyclohexanediol, a "minidetergent"

of cilia, and time-lapse imaging was performed after rapamycin addition. Micrographs at select time points are shown on the left, and the integrated intensity of ciliary GFP for the same cell is plotted on the right. 8/8 cells analyzed showed progressive entry of GFK-FKBP from base to tip. AU, arbitrary unit. (D) Fusions of GFP-FKBP with proteins of increasing size reveal the existence of a permeability barrier in live cells. All images were captured by live microscopy 6 min after rapamycin addition. Insets show enlarged views of cilia, and the yellow brackets in the last two images indicate the position of the cilium. Tetra[FKBP-MBP-GFP] denotes FKBP-MBP-GFP fused to a tetramerizing version of the Gcn4 coiled coil (Harbury et al., 1993). Bars: (main images) 5 µm; (insets) 1 µm.

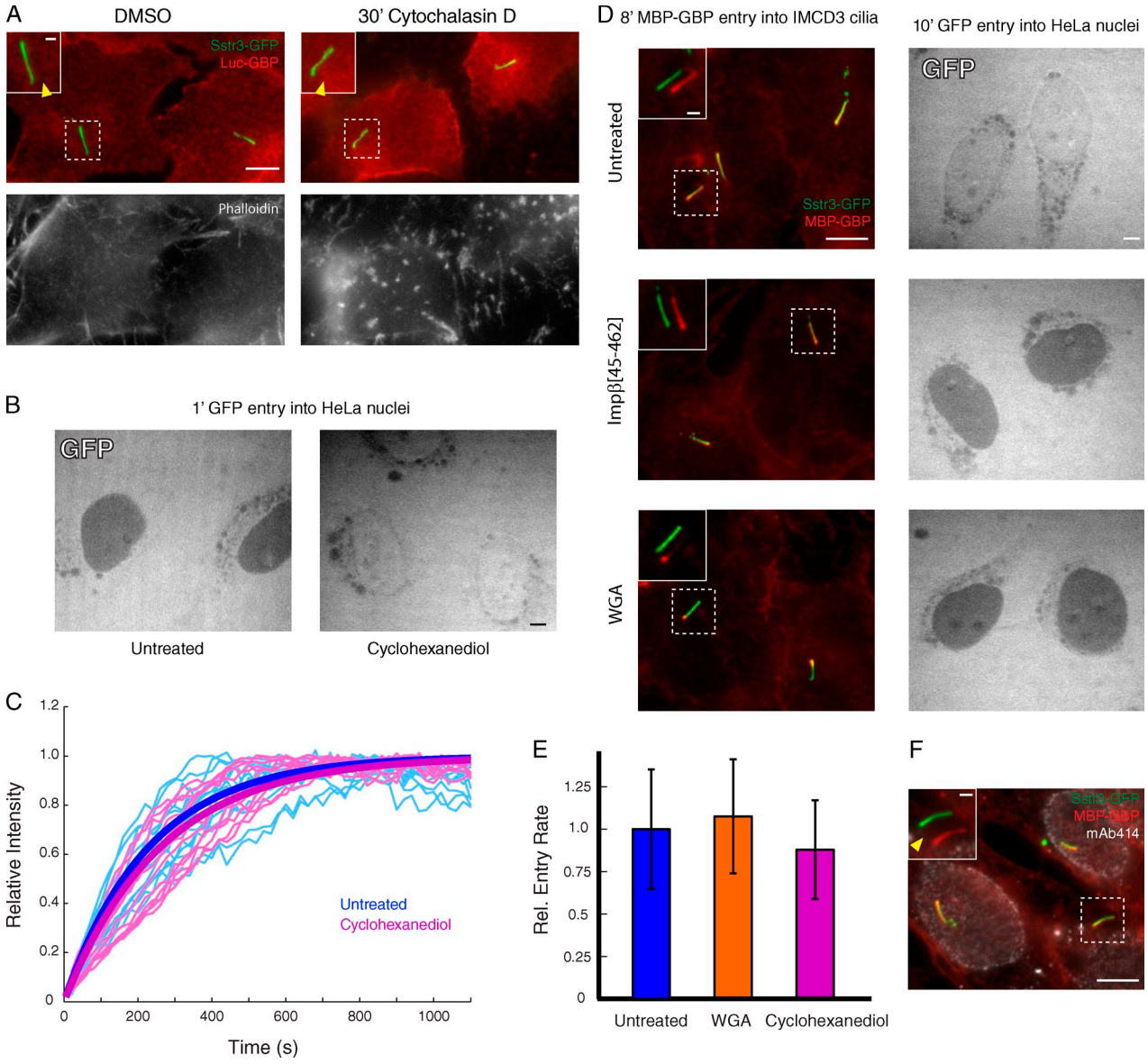

Figure 5. **The ciliary diffusion barrier is distinct from the barriers at the axon initial segment and the NPC.** (A) Cells were treated with 4 µM Cytochalasin D for 30 min to depolymerize actin before digitonin permeabilization and incubation with Luc-GBP for 10 min. Arrowheads point to the base of the cilium in the GBP channel. (bottom) F-actin (phalloidin staining), with the gain increased in untreated cells relative to Cytochalasin D–treated cells for clarity. (B) Entry of GFP (shown in white) into nuclei of digitonin-permeabilized HeLa cells was assessed in the presence and absence of 5% wt/vol 1,2-trans-cyclohexanediol. (C) The rate of MBP-GBP entry into cilia of digitonin-permeabilized IMCD3 cells was assessed in the presence and absence of 5% wt/vol cyclohexanediol. Traces for individual cilia are shown as thin lines ($n \geq 10$). Fitted exponential curves corresponding to the mean entry rates are shown as thick lines. (D) Effect of 4 µM dominant-negative Importin-β (residues 45–462) and 75 µg/ml WGA on entry of GFP into nuclei of digitonin-permeabilized HeLa cells (right) and on entry of MBP-GBP into cilia of digitonin-permeabilized IMCD3 cells (left). (E) Comparison of rates of MBP-GBP capture at the proximal segment of primary cilia for untreated cells and cells treated with WGA or 1,2-trans-cyclohexanediol. Error bars indicate standard deviations ($n \geq 10$). Rel., relative. (F) Effect of anti-Nup antibody mAb414 on MBP-GBP entry into cilia of digitonin-permeabilized IMCD3 cells. The arrowhead points to the cilium base in the mAb414 channel, where no staining is seen. Bars: (main images) 5 µm; (insets) 1 µm. All insets show primary cilia with channels shifted to aid visualization.

that disrupts hydrophobic interactions within the NPC hydrogel and thereby accelerates passive entry into HeLa cell nuclei (Fig. 5 B; Ribbeck and Görlich, 2002). However, cyclohexanediol treatment has no effect on the rate of MBP-GBP entry into IMCD3 cilia (Fig. 5, C and E). A similar lack of effect on ciliary entry is also seen with two potent inhibitors of entry into the nucleus: a truncated form of the nuclear transport factor Importin-β (Impβ(45–462); Kutay et al., 1997) and the lectin WGA, which binds and cross-links *N*-acetylglucosamine–modified Nups (Finlay et al., 1987). As previously reported (Mohr et al., 2009), both Impβ(45–462) and WGA block GFP entry into HeLa nuclei (Fig. 5 D, right), but neither reagent prevents ciliary entry of MBP-GBP (Fig. 5 D, left). Although we did observe a marked change in the distribution of MBP-GBP along the cilium in WGA-treated cells (Fig. 5 D and see Figs. 7 and 8), kinetic analysis confirmed that the rate of MBP-GBP arrival in the proximal cilium is unaffected by WGA (Figs. 5 E and S4 A).

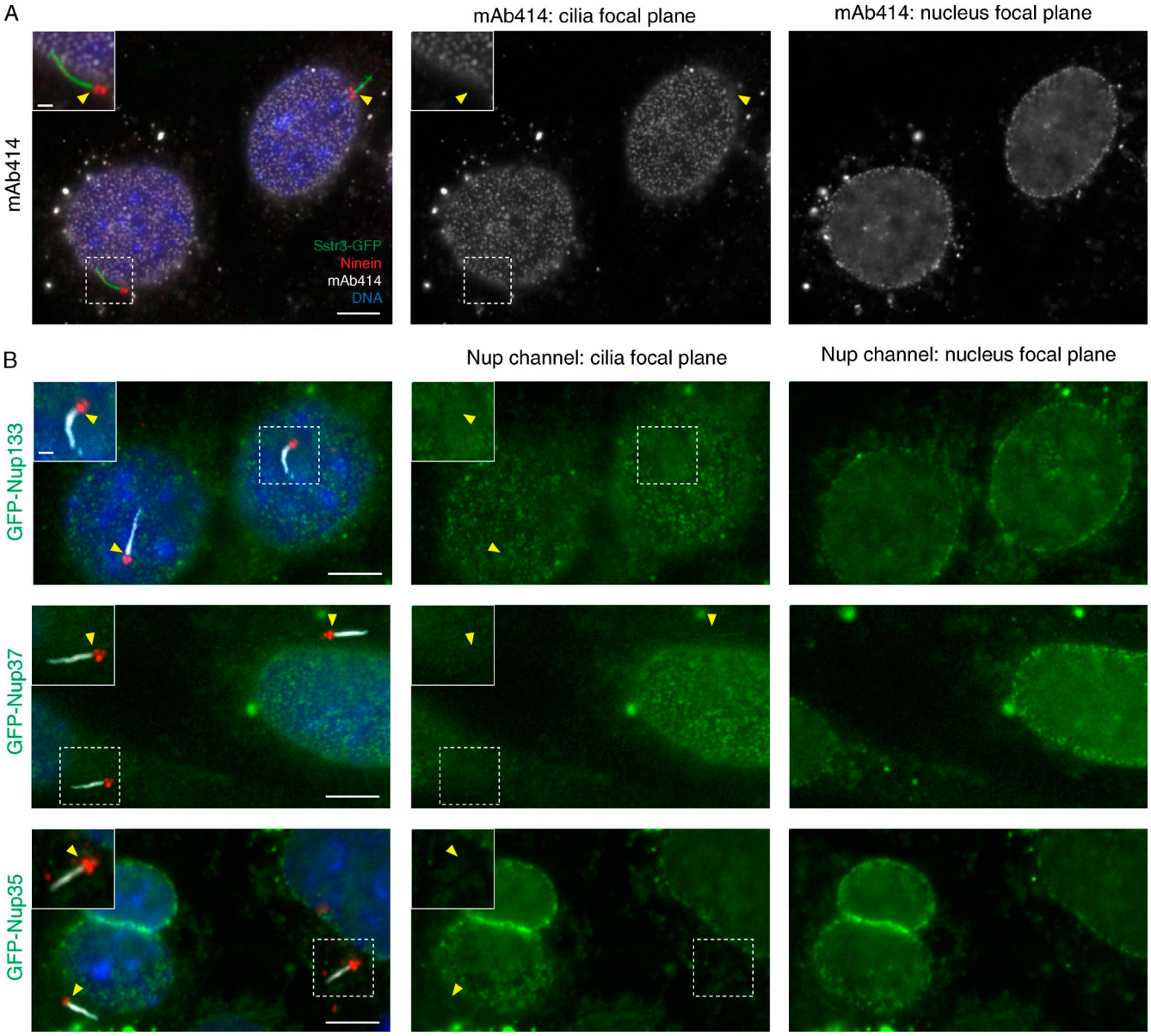

Figure 6. **Nups are not detected near the base of the cilium.** (A) IMCD3 cells were stained with anti-Nup monoclonal antibody mAb414 and an anti-ninein antibody to mark the base of the cilium. Insets show enlarged view of cilium, and arrowheads point to the base of the cilium, where no mAb414 staining is seen. (B) Nup133, Nup35, and Nup37 fused to GFP were transfected into IMCD3 cells for 48 h before processing for immunofluorescence. (right) All tested Nups localize efficiently to NPCs, as seen by spotted circles in midnuclear focal sections. (left) The centrioles and basal bodies were visualized with ninein and cilia stained with acetylated tubulin. Insets show enlarged views of cilia, and arrowheads point to the base of cilia, where no concentration of GFP signal is observed (middle). Bars: (main images) 5 µm; (insets) 1 µm.

As another means to assess the role of Nups in the ciliary diffusion barrier, we used the mAb414 antibody, which recognizes several FG-containing Nups and inhibits nuclear import (Davis and Blobel, 1986, 1987; Michaud and Goldfarb, 1992; Marshallsay and Lührmann, 1994). As seen for Impβ(45–462) and WGA, mAb414 did not inhibit MBP-GBP entry into cilia, despite prominently labeling the nuclear envelope of digitonin-permeabilized cells (Fig. 5 F).

Finally, we did not detect any mAb414-reactive Nups at or near the base of IMCD3 cell primary cilia by conventional immunofluorescence staining (Fig. 6 A). Furthermore, expression of three different Nups fused to GFP revealed no localization to the base of cilia, whereas targeting to the NPC was consistently robust (Fig. 6 B). These Nups belong to distinct subcomplexes of the central NPC scaffold (Hoelz et al., 2011) that had been proposed to localize to the base of the cilium (Kee et al., 2012). Although this difference in localization may be a result of differences in cell types, we note that GFP alone has a weak tendency to accumulate around centrosomes (Fig. S4 B and Fig. 4 B). Collectively, our data indicate that the ciliary diffusion barrier is distinct from the barriers present at the axon initial segment or the NPC.

WGA binds and immobilizes ciliary Sstr3-GFP

In digitonin-permeabilized cells incubated with WGA, we found that GBPs are restricted to the proximal region of the cilium

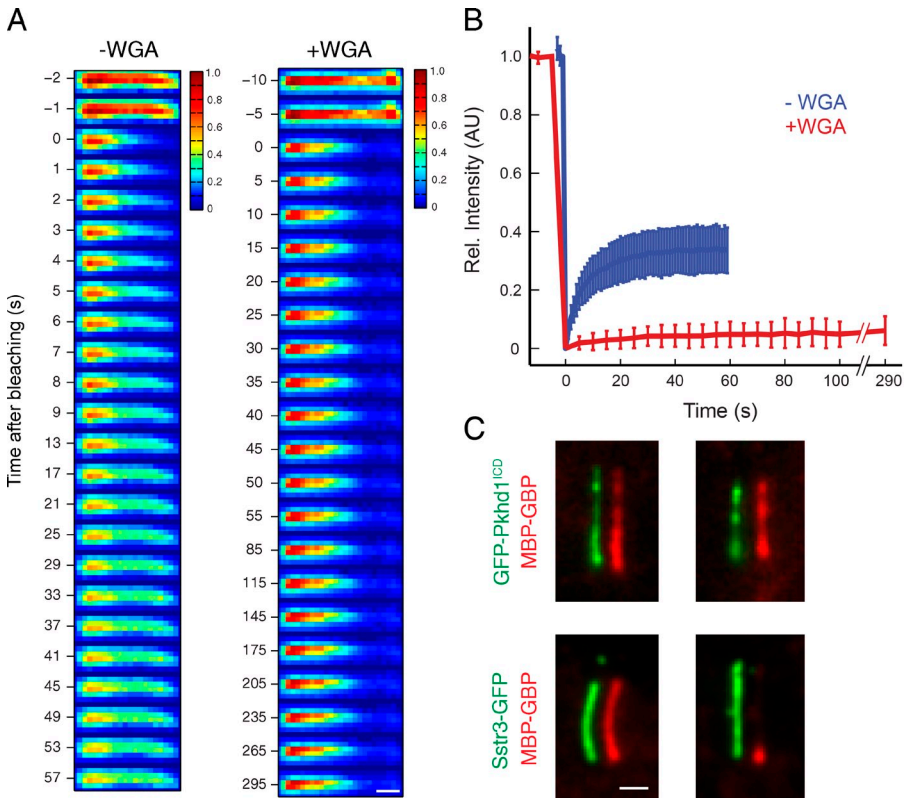

Figure 7. **WGA binds and immobilizes Sstr3-GFP in cilia.** (A) FRAP analysis of Sstr3-GFP mobility in untreated cells and cells treated with 75 µg/ml WGA. The relative (Rel.) Sstr3-GFP intensity is displayed in pseudocolored images before and after bleaching the distal half of the cilium. (B) Averaged fluorescence recovery traces for the bleached half of the cilium are plotted for untreated cells and cells treated with 75 µg/ml WGA. Error bars indicate standard deviations ($n \geq 20$). AU, arbitrary unit. (C) The effect of WGA on MBP-GBP progression within cilia was compared for cells expressing GFP fused to Sstr3 (bottom) or the lipidated cytoplasmic tail of Pkhd1 (Pkhd1^{ICD}; top). GFP and MBP-GBP channels are offset for clarity. Bars, 1 µm.

(Fig. 5 D). In evaluating the mechanistic basis for this effect, we asked whether WGA might bind directly to Sstr3-GFP. Many membrane proteins contain *N*-acetylglucosamine and sialic acid moieties recognized by WGA, and Sstr3 is highly glycosylated and captured by WGA-derivatized resin (Händel et al., 1999; Nehring et al., 2000). Furthermore, because it is a multivalent lectin (Nagata and Burger, 1974), WGA may cross-link and immobilize Sstr3, as reported previously for red blood cell glycoproteins (Golan et al., 1986). Indeed, half-cilium FRAP of Sstr3-GFP confirms that WGA prevents the lateral movement of ciliary Sstr3 in permeabilized cells (Fig. 7, A and B), as it does in live cells (Ye et al., 2013).

To rule out the possibility that WGA alters the GBP progression within cilia through a Nup-related mechanism, we incubated cells with WGA and washed out excess lectin before digitonin addition. Under these conditions, WGA cannot bind to intracellular Nups, but a proximal bias of GBP staining is still observed (Fig. S5 A). We also found a proximal-shifted GBP distribution in cells treated with *Maackia amurensis* lectin, which recognizes sialic acid–containing glycans (Knibbs et al., 1991) and does not bind Nups (Fig. S5 B; Emig et al., 1995). Lastly, we found no effect of WGA on the GBP distribution when GFP is displayed in cilia via the Pkhd1^{ICD}, which is not glycosylated (Fig. 7 C). Collectively, these data show that WGA reduces the mobility of Sstr3-GFP, which in turn influences the distribution of Sstr3-GFP:GBP complexes within cilia.

Properties of GBP diffusion to capture in the presence of WGA

How does immobilization of Sstr3-GFP modulate GBP capture inside cilia? The rapid progression of GBPs toward the cilium tip in the absence of WGA suggests that Sstr3 mobility accelerates GBP appearance in the distal portion of the cilium. In particular, diffusion within the ciliary membrane may enable Sstr3-GFP:GBP complexes that form in the proximal region of the cilium (near the site of GBP entry) to move toward the tip (Fig. 8 A, left). However, when Sstr3-GFP movement is blocked by WGA, GBPs entering cilia will be captured and immobilized at binding sites near the base, and only after these proximal GBP binding sites are saturated will GBPs gain access to more distal receptors (Fig. 8 A, right).

Consistent with this model, GBP staining in WGA-treated cells extends to increasingly distal regions of the cilium with longer staining times (Fig. 8 B). Furthermore, sequential incubation of WGA-treated cells first with Alexa Fluor 568–GBP and then with Alexa Fluor 647–GBP gives rise to two nonoverlapping domains of staining in which Alexa Fluor 568–GBP is found proximally and Alexa Fluor 647–GBP is found immediately distal to the first segment (Fig. 8 C, right). In cells not treated with WGA, free lateral movement of Sstr3-GFP:GBP complexes allows both GBPs to become evenly distributed along the entire cilium (Fig. 8 C, left).

To obtain a quantitative understanding of how Sstr3-GFP mobility impacts GBP entry and movement within cilia, we assessed the kinetics, concentration dependence, and spatial distribution of GBP staining in WGA-treated cells. For each condition, line intensity plots from base to tip were used to measure the length of the cilium stained by GBP (Fig. 9, A and B). From this analysis, we found that the square of the stained length increases linearly with time (Fig. 9 C). Furthermore, the rate of increase (i.e., slope) is proportional to the concentration

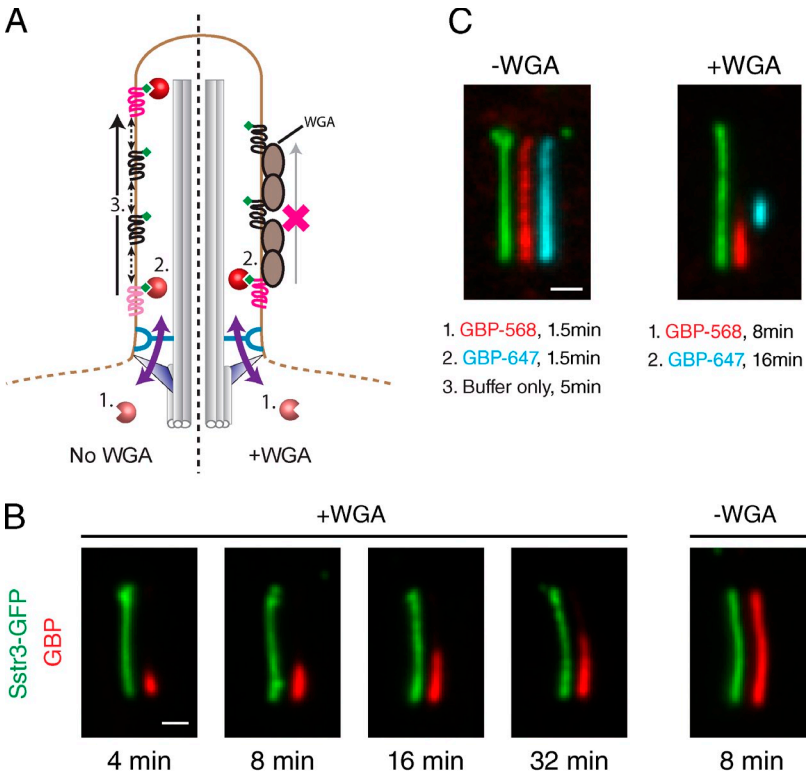

Figure 8. **Effect of WGA on GBP diffusion to capture inside IMCD3-(Sstr3-GFP) cilia.** (A) Schematic illustrating GBP behavior in untreated and WGA-treated cells expressing Sstr3-GFP. (left) In the absence of WGA, GBPs enter cilia at the base and are captured by proximal Sstr3-GFP molecules. Rapid lateral diffusion of Sstr3-GFP and Sstr3-GFP:GBP complexes enables the GBP signal to spread distally and replenishes the pool of unliganded Sstr3-GFP near the ciliary base. (right) In the presence of WGA, lateral movement of Sstr3-GFP and Sstr3-GFP:GBP complexes is blocked, and GBP signal remains concentrated at the base until proximal receptors are saturated. (B) Kinetic analysis of GBP staining of WGA-treated cells (left) or untreated cells (right). After incubation with Alexa Fluor 647–labeled GBP for the indicated times, cells were washed and fixed. Channels are offset for clarity. (C) Colorimetric pulse–chase analysis of GBP capture by ciliary Sstr3-GFP in untreated and WGA-treated cells. After digitonin permeabilization, cells were first incubated with Alexa Fluor 568–GBP and then washed and incubated with Alexa Fluor 647–GBP. Channels are offset for clarity. Bars, 1 µm.

of GBP added (Fig. 9 C). Similar results were obtained for thioredoxin (Trx)-GBP and MBP-GBP but with reduced rates (Fig. 9 F). This relationship between the length stained and time suggests that diffusion within cilia has a prominent role in our diffusion-to-capture assay, a possibility we examine by mathematical modeling.

Mathematical modeling of diffusion to capture within the cilium

We developed a mass transport model for the entry and movement of soluble GBPs within the cilium. Our model comprises concentration-dependent GBP entry into cilia, one-dimensional diffusion within cilia, and instantaneous capture by mobile or immobile Sstr3-GFP (Fig. 9 D). The motion of GBP is given by the standard diffusion equation

$$\frac{\partial B}{\partial t} = D_B \frac{\partial^2 B}{\partial x^2}, \tag{1}$$

in which B is the concentration of free GBP, D_B is its diffusion constant, and x is the position within the cilium. The flux of GBP entering through the barrier at the base of the cilium is modeled as a first-order kinetic process, occurring with a net rate proportional to the difference in GBP concentrations inside and outside the cilium, with rate constant k. At the base ($x = 0$), the flux of entering GBPs, J, is equal to the diffusional flux of GBPs, as derived from Fick's law:

$$J(x=0) = k\left[B_0 - B\left(x=0,t\right)\right] = -D_B \frac{\partial B}{\partial x}\left(x=0\right). \tag{2}$$

Here, B_0 is the cytoplasmic concentration of GBP, assumed to be constant over time.

Our model assumes that the binding of GBP to Sstr3-GFP is irreversible and diffusion limited; indeed, GBP binds GFP with a K_d of ~0.5 nM, and the half-life for complex dissociation is ~80 min (Kirchhofer et al., 2010). Consequently, free Sstr3-GFP can never coexist with unbound GBP at the same location, and the cilium can be divided into two regions: a proximal region containing free GBP and a distal region containing free Sstr3-GFP. The boundary between these two regions serves as the site of Sstr3-GFP:GBP complex formation and moves from the base to the tip as more GBP molecules enter the cilium. The boundary position, $L(t)$, is defined such that the concentration of free GBP at $L(t)$ is 0:

$$B\left[x = L\left(t\right), t\right] = 0. \tag{3}$$

When Sstr3-GFP is immobilized by WGA, free GBP arriving at the boundary binds to available receptors, gradually depleting free Sstr3-GFP and causing the boundary to move toward the cilium tip. In a given time interval, the number of GBP molecules arriving at the boundary equals the number of newly occupied Sstr3-GFPs, which can be calculated from the product of two measureable properties: the distance the boundary is displaced distally and the Sstr3-GFP concentration per unit length (S_0):

$$J(x=L) = -D_B \frac{\partial B}{\partial x}\left(x=L\right) = S_0 \frac{\partial L}{\partial t}. \tag{4}$$

We solve Eqs. 1, 2, 3, and 4 using standard techniques developed for dealing with analogous moving boundary diffusion problems (see Materials and methods; Crank, 2001). The solution exhibits two distinct behaviors of the boundary motion in different time regimes:

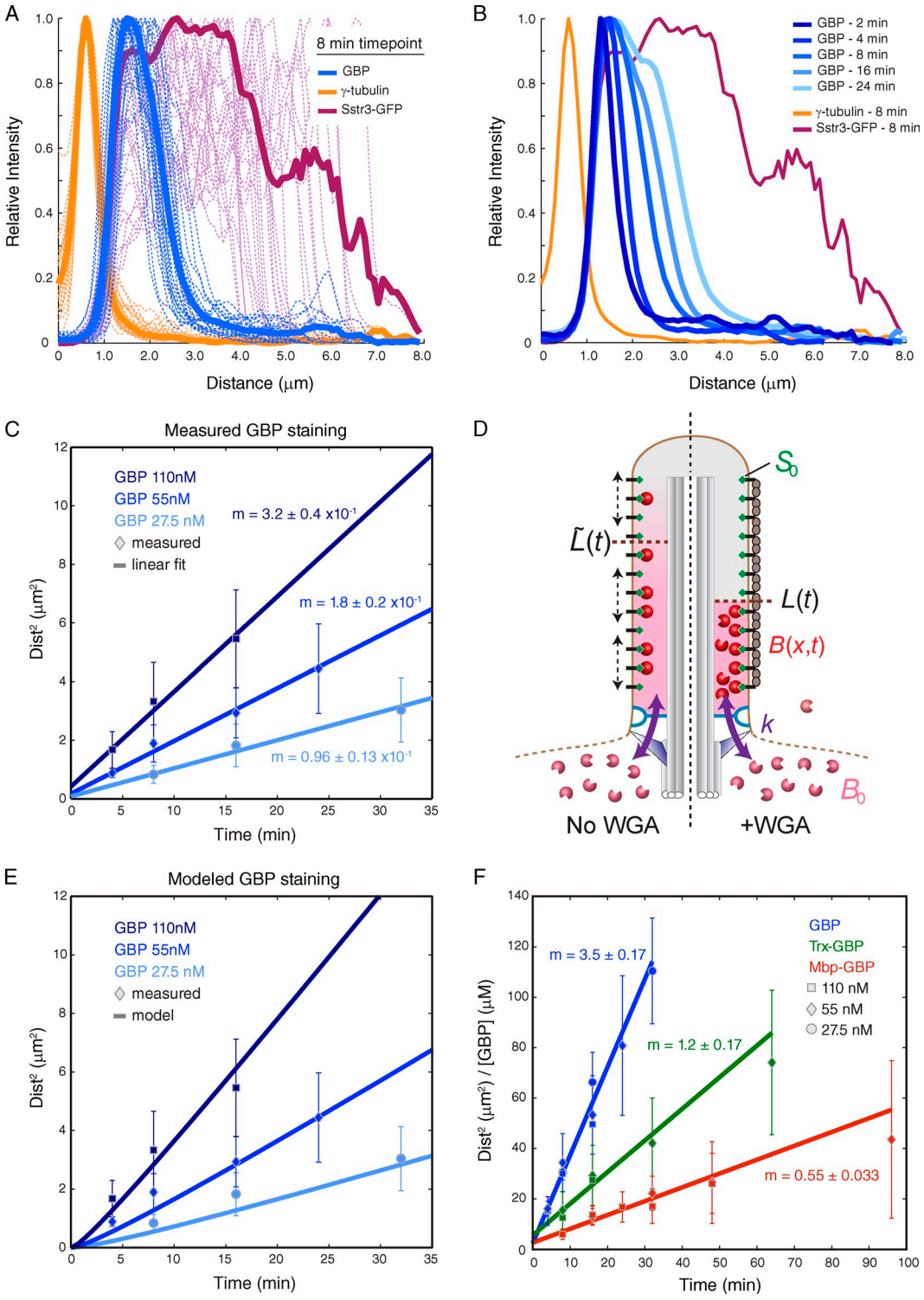

Figure 9. **Quantitative analysis of diffusion to capture in WGA-treated cells.** (A) Line traces are plotted for γ-tubulin signal, Sstr3-GFP signal, and GBP signal along the length of cilia after an 8-min incubation with 55 nM GBP. Traces for individual cilia are plotted as thin dotted lines. Averaged traces are shown as solid lines ($n \geq 20$). (B) Line traces are plotted as in A for incubations with 55 nM GBP for the indicated times. Sstr3-GFP and γ-tubulin plots correspond to the 8-min time point (n = 10–38). (C) Relationship between the square of the GBP-stained distance and time for GBP added at the indicated concentrations. Error bars indicate standard deviations (n = 10–38). The linear slope ± SEM (in micrometers squared/minute) was determined for each concentration by weighted least-squares fitting. (D) Overview of mathematical model for GBP entry into cilia and capture by Sstr3-GFP in the absence (left) and presence (right) of WGA. GBP added at concentration B_0 enters cilia with rate constant k and is captured by Sstr3-GFP present at concentration S_0. The position of the distal boundary of the GBP-stained segment is expressed as $L(t)$ (with WGA) or $\tilde{L}(t)$ (no WGA), and the position- and time-dependent concentration of free GBP within cilia is expressed as $B(x,t)$. (E) Comparison of observed GBP staining results with fitted curves derived from mathematical model using D_{GBP} = 7.3 μm²/s. (F) Relationship between time and (GBP distance stained)²/[GBP] (in micrometers squared/micromolar GBP) for GBP alone, Trx-GBP, and MBP-GBP. Data point symbols indicate the GBP concentration added. Error bars indicate standard deviations (n = 10–38). Lines show linear fits to measured data, with slopes indicated in micrometers squared/micromolar/minute.

$$L(t)=\begin{Bmatrix}\frac{B_0}{S_0}kt, & t<<t^*\\ \sqrt{\frac{2B_0D_Bt}{S_0}}, & t>>t^*\end{Bmatrix}, \text{ in which } t^*=\frac{S_0D_B}{2B_0k^2}. \quad (5)$$

For short times, the motion is limited by entry of free GBP through the barrier at the base of the cilium. At long times, the boundary movement is dominated by diffusion of free GBP past the proximal region of occupied receptors to reach free Sstr3-GFPs. In this regimen, the square of the boundary position scales linearly with time and with the cytoplasmic GBP concentration $L^2(t) = 2[B_0/S_0]D_Bt$. Note that this expression closely resembles canonical one-dimensional diffusion, $<L^2> = 2Dt$, but with a scaling factor that accounts for the relative concentrations of GBP and Sstr3-GFP. The transition between the two regimes occurs at time t^*, corresponding to the time needed for the concentration of free GBP at the cilium base to equilibrate with the cytoplasmic concentration.

To evaluate whether this model accounts for the observed rate and distance dependence of GBP staining, we used a recent tomographic study (Gilliam et al., 2012) to estimate the geometry of the cilium, and we determined the only other parameters not directly known: S_0, the concentration of Sstr3-GFP in the ciliary membrane; k, the rate constant for GBP entry; and D_B, the diffusion coefficient for GBP within the cilium. By comparing Sstr3-GFP fluorescence to a viral particle reference standard possessing 120 GFP molecules (Charpilienne et al., 2001; Joglekar et al., 2008), we found that S_0 = 6,540 ± 2,340 Sstr3-GFP molecules per micrometer length of the cilium (Fig. S5 C). We used this density together with the kinetics of GBP entry measured in Fig. 3 D to determine the initial rate of GPB entry in molecules per second and thereby calculate k (see Materials and methods).

With these values known, we obtain D_B by fitting the observed L^2 versus t data (Fig. 9 C) to the model described by Eq. 5. The resulting diffusion coefficient for GBP within the cilium equals 7.3 ± 2.8 μm^2/s. Interestingly, this value is comparable to cytoplasmic diffusion coefficients that have been measured for proteins of similar size (Elowitz et al., 1999; Luby-Phelps, 2000; Dix and Verkman, 2008), implying that the ciliary environment does not significantly slow down the motion of a small protein. It should also be noted that the transition time t^* is ∼33 s, confirming that our experimental measurements fall in the long-time regime.

To assess the accuracy of our model, we plotted the time course of GBP progression into cilia of WGA-treated cells using Eq. 5 and the derived values for B_0, S_0, k, and D_B and compared the results to those obtained experimentally. Importantly, we find a close agreement between the modeled and observed results (P = 0.984 using an F test of the null hypothesis that the model fits the data; Fig. 9, C and E). Thus, a basic mass transport system can accurately describe soluble protein entry and movement within cilia of permeabilized cells.

For the case with mobile Sstr3-GFP, we developed an analogous reaction diffusion model that includes diffusion of Sstr3 through the cilium (see Materials and methods). This model reveals that the approximate GBP boundary position is given by $\tilde{L}(t) \approx \sqrt{D_S t}$, in which D_S is the Sstr3 diffusion coefficient. Notably, when Sstr3-GFP can diffuse freely, the boundary motion is dictated by diffusion of Sstr3 rather than the motion of free GBP. Furthermore, comparison with Eq. 5 indicates that GBP progression along the length of the cilium is expected to be significantly faster in the case of mobile Sstr3-GFP even though the diffusion constant is smaller for the transmembrane protein ($D_S < D_B$). This effect, observed in Fig. 8 B, arises because the high concentration of Sstr3-GFP relative to GBP acts as a GBP sink that slows boundary movement in the WGA-treated case. Collectively, we find that a mathematical model accurately describes our experimental results and makes it possible to determine key physical properties of ciliary proteins.

Discussion

We have developed a permeabilized cell system that enables the quantitative analysis of protein entry into primary cilia. Several lines of evidence confirm that digitonin selectively permeabilizes the plasma membrane but not the ciliary membrane. First, antibodies cannot access antigens inside cilia of digitonin- or PFO-permeabilized cells but can recognize cytosolically exposed epitopes. Second, large (but not small) GBPs fail to access ciliary Sstr3-GFP after digitonin permeabilization despite readily recognizing plasma membrane Sstr3-GFP. Lastly, kinetic experiments confirm that small GBPs appear first near the base of cilia before gaining access to more distal regions.

By measuring flux into cilia of semipermeabilized cells, we resolve two conflicting studies (Kee et al., 2012; Najafi et al., 2012) and demonstrate that mammalian primary cilia possess a permeability barrier that restricts the entry of soluble proteins in a size-dependent manner. This barrier is evident from the reduction in entry rate as protein size increases, with entry not detectable for proteins with >9 nm hydrodynamic diameter (MM ∼100 kD). The agreement between our permeabilized cell system and in vivo studies by us (Fig. 4) and others (Lin et al., 2013) provides further support for the validity of our in vitro system. For soluble proteins found within cilia that are close to or above the passive diffusion limit (e.g., tubulin dimers, molecular motors, and Gli transcription factors), active transport mechanisms must be required for efficient ciliary targeting. Given that the transport of soluble proteins needs to overcome different constraints than those imposed on membranous cargoes, the identification of the targeting signals present on these ciliary proteins and of the transport machinery that recognizes these signals will be key goals for future studies. Furthermore, it will be critical to determine how trans-acting factors carry large cargoes across the ciliary permeability barrier. To gain mechanistic insights into these fundamental questions, a reconstituted transport system in semipermeabilized cells may provide a unique tool, enabling a range of experimental manipulations not possible in live cells. In particular, the reactivation of IFT observed upon addition of cellular extracts and ATP (Fig. 2 B) offers an appealing system for the mechanistic dissection of IFT-mediated trafficking.

Although the molecular basis of the ciliary permeability barrier awaits further characterization, our data demonstrate that this barrier is distinct from those present at the axon initial segment or the NPC. This latter finding is in contrast to a recent study indicating that Nups at the base of cilia restrict protein entry (Kee et al., 2012). Because Nup-regulated ciliary entry was only functionally supported for kinesin Kif17 (MM = 116 kD), it is possible that our divergent conclusions reflect mechanistic differences between passive diffusion and active transport. Nonetheless, the absence of detectable Nups at the transition zone in IMCD3 cells (Fig. 6) makes this possibility unlikely.

In addition to outstanding questions regarding the molecular basis of the ciliary diffusion barrier, the ultrastructural organization of the barrier is also unknown. The two most distinctive structural elements found at the base of cilia are the transition zone Y links and the transition fibers (Nachury et al., 2010; Reiter et al., 2012). However, neither of these elements is known to constrict to <40 nm. It is therefore likely that the ciliary diffusion barrier is not readily seen by electron microscopy and that new approaches will be needed to characterize its structural features.

Our permeabilized cell system also enabled the measure of key physical properties for ciliary proteins. Specifically, FRAP analysis and a quantitative model for GBP entry made it possible to determine diffusion coefficients for both transmembrane and soluble proteins inside mammalian primary cilia. Notably, because IFT movement stops in permeabilized cells, our measurements reflect diffusion alone and are not impacted by active transport. We find that diffusion within primary cilia is not significantly reduced relative to the cytoplasm, a result in agreement with studies on diffusion of macromolecules and metabolites in sperm flagella and frog photoreceptors (Takao and Kamimura, 2008; Calvert et al., 2010). Specifically, our observed ciliary diffusion coefficients (0.2 $\mu m^2/s$ for Sstr3-GFP and 7 $\mu m^2/s$ for GBP) are similar to reported values for protein diffusion in the plasma membrane ($\sim$0.1–0.4 $\mu m^2/s$) and the cytoplasm ($\sim$1–20 $\mu m^2/s$; Elowitz et al., 1999; Luby-Phelps, 2000; Calvert et al., 2001; Suzuki et al., 2005; Dix and Verkman, 2008; Chung et al., 2010; Jaqaman et al., 2011). Interestingly, these diffusion coefficients indicate that soluble and membrane proteins can travel the roughly 4-µm distance from ciliary base to tip in <5 and $\sim$30 s, respectively, time scales comparable to IFT-mediated transport ($\sim$0.5–1.5 µm/s; unpublished data; Follit et al., 2006; Tran et al., 2008; Besschetnova et al., 2009).

It is therefore possible that IFT complexes are not strictly required for rapid protein movement within cilia. For example, consider a scenario in which tubulin incorporation at the tip of the axoneme is limited solely by the rate of diffusional arrival of tubulin from a pool near the base (analogous to GBP capture by immobilized Sstr3-GFP). In this case, at steady-state, there would be a linear concentration profile of free tubulin from base to tip, and the rate of arrival at the cilium tip would be proportional to the tubulin concentration at the base. Additionally, the arrival rate would be inversely proportional to cilium length, a relationship also predicted by the balance point model for ciliary length regulation proposed by Marshall et al. (2005). Furthermore, a tubulin concentration near the base of $\sim$0.5 µM (with $D_{tubulin}$ = 1 $\mu m^2/s$) would allow diffusional flux to sustain a cilium of length of $\sim$5 µm and offset continuous turnover of axonemal tubulin (Marshall et al., 2005). Such a model is also consistent with the recent finding that soluble tubulin levels regulate cilium length (Sharma et al., 2011).

Although the regulation of axoneme growth is likely to be considerably more complex in vivo and may use IFT (Hao et al., 2011), our observations nonetheless underscore the need for a better understanding of which ciliary processes are dependent on active transport and which are supported by simple diffusion. The importance of diffusion is highlighted by the recent finding that, in specific genetic contexts, seemingly null mutations in dynein 1b permit normal Hedgehog signaling and cilium assembly (Ocbina et al., 2011) and by the observation that normal cilium morphology is maintained upon acute inactivation of dynein 1b (Engel et al., 2012). In the presence of such dynein mutations, protein movement from tip to base of cilia—to recycle damaged proteins or transmit Hedgehog signals to the cell body—is likely to rely on passive diffusion. Meanwhile, anterograde IFT is indispensable for cilium assembly, likely because of the large amounts of materials that must be delivered to the tip of cilia during axoneme elongation (Ishikawa and Marshall, 2011). IFT may also carry out alternative functions such as promoting the active entry of large proteins into cilia (Pedersen and Rosenbaum, 2008) or participating in scaffolding signal transduction cascades, as suggested by the work of the Snell group on IFT-dependent signaling in flagella of *Chlamydomonas reinhardtii* (Wang et al., 2006). In future studies, the permeabilized cell system presented here will likely provide a valuable tool for dissecting active transport processes and their contributions to ciliary function.

Materials and methods

Antibodies and reagents

The following antibodies were used for immunofluorescence staining: goat anti-GFP (#600-101-215; Rockland Immunochemicals), mouse anti–S tag (#71549; EMD), mouse antimyc (#sc-40; Santa Cruz Biotechnology, Inc.), rabbit anti-Arl13b (gift from T. Caspary; Emory University, Atlanta, GA), mouse anti–acetylated α-tubulin (#T6793; Sigma-Aldrich), mouse anti–γ-tubulin (#T6557; Sigma-Aldrich), mouse anti-Nup mAb414 (#MMS-120R; Covance), and rabbit antininein (gift from M. Bornens, Institut Curie, UMR144 du Centre National de la Recherche Scientifique, Paris, France). Alexa Fluor 546–labeled phalloidin was purchased from Invitrogen (#A22283). WGA (#L9640 and #L5142), Cytochalasin D (#C8273), cyclohexanediol (#141712), creatine kinase (C3755), phosphocreatine (P7936), and ATP (A7699) were purchased from Sigma-Aldrich. High-purity digitonin (#300410) and rapamycin (#553211) were purchased from EMD Millipore.

Cell culture

IMCD3 cells were cultured in DMEM/F12 medium (Life Technologies) containing 10% FBS (HyClone) at 37°C in 5% CO_2. To induce ciliogenesis, cells were grown in serum starvation medium (0.2% FBS) for 24 h. Clonal stable cell lines expressing Sstr3-S-GFP, GFP-S-IFT88, GFP-Pkhd1^{ICD}, and Sstr3-TagRFP-T-FRB under control of the EF1-α promoter were generated using the Flp-In system (Invitrogen) as described previously (Jin et al., 2010). Plasmids encoding TagRFP-T, Sstr3, and the FRB/FKBP domains were provided by R. Tsien (University of California, San Diego, La Jolla, CA), K. Mykytyn (The Ohio State University, Columbus, OH), and T. Meyer (Stanford University, Stanford, CA), respectively. Where indicated, cells were transfected using Lipofectamine 2000 (Life Technologies) with tagged Nups (gift from M. Hetzer, Salk Institute for Biological Studies, La Jolla, CA),

the pericentrin-AKAP450 centrosomal targeting domain from pericentrin (gift from S. Munro, Medical Research Council Laboratory of Molecular Biology, Cambridge, England, UK; Gillingham and Munro, 2000) or with FKBP fusions, including the tetramerizing coiled coil from Gcn4 (gift from K.C. Garcia, Stanford University, Stanford, CA).

Cell extracts

Cytosolic extract from bovine retina was prepared as previously described (Jin et al., 2010). In brief, frozen retinas (W L Lawson Co.) were thawed in breaking buffer (25 mM Hepes, pH 7.4, 150 mM KOAc, 210 mM sucrose, 2 mM $MgCl_2$, 2.5 mM $CaCl_2$, and 5 mM EGTA) supplemented with protease inhibitors. After dounce homogenization and removal of cell debris by centrifugation at 1,000 *g*, the lysate was centrifuged for 1 h in a rotor (TLA100.3; Beckman Coulter) at 100,000 *g*. The resulting supernatant was supplemented before use with an ATP-regenerating system containing 1 mM ATP, 5 mM phosphocreatine, and 40 U/ml rabbit muscle creatine kinase. Cytosolic extract from *Xenopus* eggs (low-speed supernatant) was prepared as described previously (Moree et al., 2011). In brief, *Xenopus* eggs were washed in MMR buffer (5 mM Hepes, 0.1 mM EDTA, 100 mM NaCl, 2 mM KCl, 1 mM $MgCl_2$, and 2 mM $CaCl_2$, pH 7.8) and dejellied in MMR with 2% L-cysteine. Eggs were then washed in CSF-XB buffer (100 mM KCl, 50 mM sucrose, 2 mM $MgCl_2$, 0.1 mM $CaCl_2$, 10 mM Hepes, and 5 mM EGTA, pH 7.7) and washed again in CSF-XB with protease inhibitors. Eggs were placed in a 13 × 51–mm ultraclear tube (Beckman Coulter) and packed by centrifugation. Excess buffer was removed before centrifugation for 15 min at 10,000 rpm in a rotor (SW55 Ti; Beckman Coulter). The soluble cytoplasmic material was then removed and supplemented with 10 mg/ml Cytochalasin D and an energy regenerating system.

Recombinant protein expression, purification, and labeling

PFO with the C459A mutation (gift from A. Johnson, Texas A&M University, College Station, TX) was expressed in Rosetta2(DE3)-pLysS cells (EMD Millipore) and purified as previously described (Shepard et al., 1998). His-tagged EGFP and His-tagged Impβ(45–462) (gift from D. Görlich, Max-Planck-Institut für biophysikalische Chemie, Göttingen, Germany) were expressed from pET vectors (EMD Millipore) in Rosetta2(DE3)-pLysS cells. Protein expression was induced with 200 µM IPTG, and cells were grown overnight at 19°C in 2YT medium. EGFP-expressing cells were lysed by sonication in 4XT buffer (80 mM Tris and 800 mM NaCl, pH 7.4) before dilution 1:1 with water. Cells expressing Impβ(45–462) were lysed in 30 mM sodium phosphate and 300 mM NaCl, pH 7.2. Proteins were purified on Ni–nitrilotriacetic acid agarose (QIAGEN) and eluted from resin with 300 mM imidazole.

DNA encoding the camelid GBP (Kirchhofer et al., 2010) was prepared by gene synthesis and cloned into a pET expression vector with a C-terminal 6×His tag. GBP fusions (except for MBP-GBP) were generated by inserting genes of interest upstream of GBP in this vector. MBP-GBP was generated by cloning GBP-6×His into the pMal-C2x MBP-tagging plasmid (New England Biolabs, Inc.). All GBP fusions were expressed in Rosetta2(DE3)-pLysS cells and grown in ZYM-5052 autoinduction medium for 18 h at 22°C. Cells were harvested by centrifugation and lysed by sonication in buffer A (20 mM sodium phosphate, pH 7.2, 500 mM NaCl, 10 mM imidazole, 0.5 mM DTT, 1% NP-40, and 10 µg/ml each of leupeptin, pepstatin A, bestatin, aprotinin, AEBSF, and E-60). Lysates were clarified by centrifugation and bound to Ni–nitrilotriacetic acid agarose. After extensive washing, GBPs were eluted in buffer A with 300 mM imidazole and loaded onto a Superdex 200 column for further purification and Stokes radius measurement. Size exclusion chromatography was performed in buffer B (20 mM Hepes, pH 7.7, 150 mM NaCl, and 0.5 mM DTT) on a purifier (Äkta; GE Healthcare). Calibration standards for Stokes radius determination were purchased from Sigma-Aldrich (blue dextran, thyroglobulin, β-amylase, BSA, and cytochrome *c*). Peak fractions were pooled and labeled with Alexa Fluor 647 or Alexa Fluor 568 succinimidyl esters according to the manufacturer's protocol (Life Technologies), and excess dye was separated from labeled protein with columns (NAP-5; GE Healthcare).

Semipermeabilization with digitonin and PFO

Coverslips with serum-starved IMCD3 cells were first placed on an ice-chilled metal block and washed twice with cold assay buffer (20 mM Hepes, pH 7.4, 115 mM KOAc, 1 mM $MgCl_2$, and 1 mM EGTA). To induce permeabilization, coverslips were incubated for 7 min in cold assay buffer supplemented with 30 µg/ml digitonin and protease inhibitors (10 µg/ml each of leupeptin, pepstatin A, bestatin, aprotinin, AEBSF, and E-60). Alternatively, coverslips were incubated on ice for 10 min in assay buffer supplemented with 50 µg/ml PFO. Unbound PFO was removed by washing with cold assay buffer, and pore formation was then induced by incubating coverslips for 15 min at 37°C in assay buffer with protease inhibitors.

After permeabilization, coverslips were washed twice with assay buffer and incubated with GBPs and/or antibodies diluted in assay buffer supplemented with 0.1% BSA. Unless otherwise indicated, incubations with GFP binders were performed for 10 min at room temperature. All GBPs were used at 55 nM for endpoint assays and at 110 nM for time-lapse imaging; antibodies were used at 2–4 µg/ml. Where indicated, rabbit IgG at 50 µg/ml was preincubated with ZZ-GBP for 10 min. For WGA treatment, cells were incubated with WGA at 75 µg/ml for 7 min immediately before GBP staining; in these cases, WGA was also included in assay buffer during staining. After staining, coverslips were washed twice with assay buffer, fixed, and processed for immunofluorescence microscopy.

Immunofluorescence microscopy

Cells grown on acid-washed 12-mm #1.5 coverslips were fixed in assay buffer containing 4% paraformaldehyde for 10 min at room temperature. For γ-tubulin staining, cells were fixed for 5 min with paraformaldehyde, extracted in −20°C methanol for 5 min, and rehydrated in PBS. After cell fixation, cells were permeabilized in PBS with 0.1% Triton X-100 for 10 min, washed twice with PBS, and blocked for 30 min in PBS with 3% BSA and 5% normal donkey serum. Cells were then incubated with primary antibodies diluted in PBS + 3% BSA for 1 h at room temperature, washed five times with PBS + 3% BSA, and incubated with Cy3- and/or Alexa Fluor 647–labeled secondary antibodies (GBPs labeled with Alexa Fluor 647 or Alexa Fluor 568) diluted in PBS + 3% BSA for 30 min. Finally, coverslips were further washed, stained with Hoechst DNA dye, and mounted on slides in 80% glycerol and 10 mM Tris, pH 7.4.

Fixed cells were imaged at room temperature at 350-nm z intervals on a microscope (Axio Imager.M1; Carl Zeiss). Epifluorescent illumination was provided by a light source (Lambda XL; Sutter Instrument) through a 63×, 1.4 NA Plan Apochromat objective. Images were captured with a camera (CoolSNAP HQ^2; Photometrics) using SlideBook software (Intelligent Imaging Innovations).

Live-cell imaging and photobleaching

For live-imaging microscopy, cells were cultured on 25-mm circular acid-washed #1.5 glass coverslips and imaged at 37°C. Permeabilized cells and viral particles were imaged in assay buffer; live cells were imaged in live-imaging medium (phenol red-free DMEM/F12 medium supplemented with 25 mM Hepes, pH 7.4).

Time-lapse imaging of GBP entry and imaging of GFP-tagged viral particles were performed through a 63×, 1.4 NA Plan Apochromat objective on an inverted microscope (TE2000; Nikon). Illumination at 488 and 647 nm was provided by a laser (Innova 70C-Spectrum; Coherent), and images were collected through a spinning-disc confocal scanner (CSU10; Yokogawa Corporation of America) and acquired with a charge-coupled device camera (Cascade 512B; Photometrics) using MetaMorph software (Molecular Devices). To minimize background signal from GBPs binding to Sstr3-GFP in the plasma membrane, permeabilized cells were preincubated with unlabeled LacZ-GBP. Images in the GFP and Alexa Fluor 647–GBP channels were acquired in five z planes with 450-nm spacing at the indicated time intervals. Cilia of permeabilized cells were identified from their GFP fluorescence, and time-lapse videos were started upon addition of GBP at 110 nM.

For analysis of ciliary entry in intact cells, GFP-FKBP fusion proteins were expressed from an EF1-α promoter via transient transfection of IMCD3 cells stably expressing Sstr3-TagRFP-T-FRB. Time-lapse imaging was performed after addition of 1 µM rapamycin; alternatively, cells were fixed after 10 min and processed for immunofluorescent staining as described previously. Time-lapse imaging of rapamycin-dependent ciliary entry and of GFP-IFT88 movement was performed on an inverted microscope (DeltaVision Elite; Applied Precision) equipped with a solid state light source (InsightSSI) and a laser module (X4) controlling a 50-mW 488-nm laser (Applied Precision). Images were captured with CoolSNAP HQ^2 or sCMOS cameras (Applied Precision) using softWoRx software (Applied Precision). TIRF images of GFP-FKBP fluorescence were acquired through a 60×, 1.49 NA Apochromat normal TIRF objective (Olympus) at 6–9-s intervals for 6 min after rapamycin addition. Additional epifluorescence and TIRF images of Sstr3-RFP-FRB and GFP-FKBP were acquired immediately before and after time-lapse imaging. For analysis of GFP-IFT88 movement, a single z plane was imaged through a 60×, 1.4 NA objective (Olympus) at 1–2 frames/s for 30 s.

FRAP and TIRF microscopy of IMCD3 Sstr3-GFP cells were performed on a microscope (Axiovert 200M; Carl Zeiss). Epifluorescence excitation through a 63×, 1.4 NA oil objective (Olympus) was provided by a Xenon lamp (DG4 300W; Sutter Instrument). TIRF excitation was provided by a 473-nm solid-state laser (CrystaLaser) and a TIRF slider (Carl Zeiss) through a 100× Plan Fluor 1.45 NA objective (Olympus). Photobleaching was performed with a FRAP laser system (MicroPoint; Photonic Instruments). Images were acquired with a camera (CoolSNAP HQ), and the system was controlled with SlideBook software. In a typical bleaching experiment, cells were imaged in a single focal plane at one frame/s for 3 s before bleaching and 60 s after bleaching. For WGA-treated cells, the interval was 0.2 frames/s.

Image analysis

All data analysis described in this section was performed using Matlab (MathWorks) and ImageJ (National Institutes of Health) software. For measurement of GBP entry rates, masks corresponding to cilia were first defined based on Sstr3-GFP signal relative to background. Minor drift in the focal plane during imaging was effectively corrected by selecting at each time point the z section with the greatest ciliary GFP signal. To measure the GBP signal at the base, the GBP intensity was computed for all 2 × 2–pixel areas near the ciliary base, and the mean of the four brightest 2 × 2 areas was used for subsequent data analysis. This GBP intensity, after subtracting the background measured from pixels neighboring the cilium, was determined at each time point and used for fitting to a single exponential equation with rate k. Fitted rates were determined separately for each cilium and averaged to determine the mean and standard deviation of the entry rate for each GBP. We note that similar results were obtained with or without photobleaching correction.

For measurement of GBP staining length in WGA-treated cells, line segments along cilia were defined in ImageJ. Intensity line profiles for each channel along the length of cilia were measured in ImageJ and aligned according to the peak of the basal body staining. The points at which the observed intensity decreased to <25% of the maximal observed intensity were used to define the start and end points of GFP and GBP signals. The length from start to end point along the cilium was measured for each cilium and averaged to obtain the mean length; normalized intensity profiles were averaged to produce a representative line profile for each condition.

For quantification of FRAP data, cilia were first identified from the prebleach Sstr3-GFP signal. For each ciliary pixel, the relative intensity before and after bleaching was determined and used to define the boundary between the bleached and unbleached region (with the boundary typically corresponding to pixels with ∼30% of prebleach intensity). Regions roughly 1 µm proximal to and distal to the boundary were used for measurement of unbleached and bleached pixel intensities. The mean signal in the bleached and unbleached regions after background subtraction was determined at each time point. The mean pixel intensity throughout the cilium was also calculated to determine the expected final intensity in the bleached region (at infinite time and with 100% receptor mobile fraction). To generate mean recovery curves, measured intensities were normalized for each cilium such that the intensity of the bleached region equals 1.0 before bleaching and equals 0.0 immediately after bleaching. The receptor mobile fraction was calculated from the observed magnitude of fluorescence recovery relative to that expected if Sstr3-GFP fluorescence were spread evenly along the cilium. The fraction of molecules within the bleached region that were successfully photobleached was determined from the relative fluorescence in the bleached versus unbleached regions immediately after bleaching. To obtain diffusion coefficients, recovery curves were first normalized such that the mean postbleach intensity in the whole cilium equals 1.0 and the background fluorescence equals 0.0. The cumulative density of bleached molecules between positions 0 and x at time t is given by

$$H(x,t) = \frac{xa}{L} + \sum_{n=0}^{\infty}\left[\frac{2L}{\pi^2 n^2}\sin\left(\frac{n\pi a}{L}\right)\sin\left(\frac{n\pi x}{L}\right)\exp\left(\frac{-\pi^2 D n^2 t}{L^2}\right)\right],$$

in which the region from 0 to a is bleached, L is the length of the cilium, and D is the diffusion coefficient. We fit the measured fluorescence intensity in a narrow segment of the cilium as a function of time after photobleaching to a model of one-dimensional diffusion in a bounded region. If f_b is the fraction of molecules bleached within the bleached region, and f_m is the fraction of molecules that are mobile, the fractional intensity measured between positions a_1 and a_2 at time t is given by

$$f = 1-(1-f_m)f_b - \frac{f_b f_m}{1-f_b a/L}\frac{\left[H(a_2 t)-H(a_1 t)\right]}{a_2-a_1}.$$

This functional form is used in a least-squares fit for the diffusion coefficient D. Fitted values for D were determined for each cilium analyzed and averaged to obtain the mean diffusion coefficient for Sstr3-GFP.

To determine the concentration of Sstr3-GFP molecules in the ciliary membrane, GFP-tagged viral particles were imaged under the same imaging conditions as used for measuring rates of GBP entry in permeabilized cells. Each particle's intensity was measured in a summed z-stack projection. After background subtraction, the mean particle intensity was used to determine the fluorescence intensity of a single GFP molecule under the imaging conditions used. Similarly, the summed z-projection intensities for cilia were measured, and the Sstr3-GFP intensity per unit length was used to determine the mean number of Sstr3-GFP molecules per micrometer length of the ciliary membrane.

Mathematical modeling of diffusion to capture

Immobile Sstr3-GFP. The transport of GBP along the cilium where the Sstr3-GFP receptors have been immobilized with WGA is described by the moving-boundary diffusion problem encompassed by Eqs. 1, 2, 3, and 4, together with the initial condition $L(0) = 0$. We note that our model assumes rapid equilibration of GBP concentration across the cilium cross section, so that only transport along the length of the cilium is considered. The solution to these differential equations is derived analogously to the moving boundary problems described by Crank (2001) and can be expressed as

$$B(x,t) = \frac{B_0}{\mathrm{Erf}\left(\frac{\xi}{2}\right)}\left\{\mathrm{Erfc}\left[\frac{x}{2\sqrt{D_B\left(t+t^*\right)}}\right] - \exp\left[\frac{xk}{D_B}+\frac{k^2\left(t+t^*\right)}{D_B}\right]\mathrm{Erfc}\left[\frac{x}{2\sqrt{D_B\left(t+t^*\right)}}+k\sqrt{\frac{t+t^*}{D_B}}\right]\right\} + B_0\left(1-\frac{1}{\mathrm{Erf}\frac{\xi}{2}}\right), \quad (6)$$

in which Erf is the error function, Erfc is the complementary error function, ξ satisfies

$$\frac{B_0\exp\left[-\xi^2/4\right]}{\sqrt{\pi}\mathrm{Erf}\left[\xi/2\right]} = \frac{\xi}{2},$$

and t^* satisfies

$$\exp\left(\frac{k^2 t^*}{D_B}\right)\mathrm{Erfc}\left(\sqrt{\frac{k^2 t^*}{D_B}}\right) = \mathrm{Erf}\left(\frac{\xi}{2}\right).$$

At short times ($t << t^*$), the front position at which the concentration of GBP hits zero moves as $L(t) = t/2t^*$. At long times ($t >> t^*$), this front moves as

$$L(t) = \xi\sqrt{\frac{k^2\left(t+t^*\right)}{D_B}}.$$

In the limiting case in which the Sstr3-GFP receptors are much more concentrated than the GBP ($S_0 >> B_0$), this solution reduces to the form given in Eq. 5.

Mobile Sstr3-GFP. If the Sstr3-GFP receptors are allowed to diffuse over the ciliary membrane, there will be an initial period during which all entering GBP is absorbed by receptors at the base, and there is no free GBP within the cilium. This period ends at time $\hat{t}$ when all the free Sstr3-GFP at the base is depleted. As explained in this section, we find that our measurements fall exclusively within the early time regimen ($t << \hat{t}$), and thus, we investigated GBP capture under these conditions. The concentration profile $S(x,t)$ of free Sstr3-GFP in this case must satisfy the diffusion equation and initial condition $\partial S/\partial t = D_S(\partial^2 S/\partial x^2)$ and $S(x, t = 0) = S_0$. Furthermore, at the entry point at the base of the cilium, the flux of disappearing free Sstr3-GFP should equal the rate of incoming GBP molecules $D_S(\partial S/\partial x) = kB_0$. The solution to these three equations is given by

$$S(x,t) = S_0 - kB_0\sqrt{\frac{4t}{\pi D_S}}\exp\left[\frac{-x^2}{4D_S t}\right] + \frac{kxB_0}{D_S}\mathrm{Erfc}\left[\frac{x}{2\sqrt{D_S t}}\right].$$

The transition time $\hat{t}$ is then found by setting $S(0, \hat{t}) = 0$, yielding

$$\hat{t} = \frac{\pi D_S}{4k^2}\left(\frac{S_0}{B_0}\right)^2.$$

In the early time regimen, all bound GFP–GBP complexes are produced at the origin, with constant rate kB_0. The bound complexes spread diffusively from the origin, with a diffusion constant that is assumed to be equal to that of free Sstr3-GFP (D_S). The density profile of the complexes is then given by

$$C(x,t) = \int_0^t \frac{kB_0}{\sqrt{\pi D_S t'}}\exp\left(\frac{-x^2}{4D_S t'}\right)dt' = kB_0\left[\sqrt{\frac{4k^2 t}{\pi D_S}}\exp\left(\frac{-x^2}{4D_S t}\right) - \frac{kx}{D_S}\mathrm{Erfc}\left(\frac{x}{2\sqrt{D_S t}}\right)\right].$$

We define the approximate distance along the cilium over which the bound complexes have spread as the position $\tilde{L}(t)$ such that 75% of the bound complex density lies between the base and $\tilde{L}(t)$. This position can then be expressed as $\tilde{L}(t) = a\sqrt{D_S t}$, in which $a \approx 1.08$ satisfies the equation

$$\frac{-a^2}{2} + \left(\frac{a^2}{2} + 1\right)\mathrm{Erf}\left(\frac{a}{2}\right) + \frac{a}{\sqrt{\pi}}\exp\left(\frac{-a^2}{4}\right) = 0.75.$$

Evaluation of model parameters

The density of Sstr3-GFP is known from the surface density of Sstr3 receptors determined in Fig. S5 C, yielding S_0 = 6.54 receptors/nm (expressed subsequently as nm^{-1}) and D_S = 0.21 $\mu m^2/s$, as measured in Fig. 2 A. To determine the rate constant for GBP entry, k, we used the relative rate of GBP entry measured in Fig. 3 D. This relative rate, k^* = 0.031 s^{-1}, can be used together with N_{base}, the estimated final number of GBP molecules near the base of the cilium, to determine V_0, the initial rate of GBP entry in molecules per second. V_0 is in turn related to k as follows: $V_0 = k^* \times N_{base} = k \times B_0$, yielding k = 28,000 nm/s when N_{base} is calculated for a 500-nm segment at the cilium base containing 500 × S_0 = 3,270 GBP binding sites.

We note that in this one-dimensional model, the variables B_0 and S_0 correspond to the linear densities of GBP and Sstr3-GFP, respectively. To calculate these linear densities from the bulk concentration requires an estimate of the cilium geometry (Gilliam et al., 2012). We treat the ciliary lumen as an annular region with an outer radius, R = 151 nm, and an inner radius, r = 78 nm (corresponding to the region excluded by the microtubule core). The density of GBP is then given by B_0 (in nm^{-1}) = 0.6 × $\pi(R^2 - r^2)[B]_0$, in which $[B]_0$ is the bulk solution concentration expressed in molars. We note that treating the ciliary lumen as a hollow tube with R = 151 nm that contains axonemal microtubules (modeled as nine 22-nm-diameter A tubules and nine 24-nm-diameter B tubules) yields similar results ($D_{annulus}$ = 7.3 $\mu m^2/s$; D_{tube} = 5.9 $\mu m^2/s$).

To extract an estimate for the diffusion constant of free GBP within the cilium, we fit all data in Fig. 9 C to the full expression for the boundary position over time, obtained by setting Eq. 6 equal to 0. The resulting diffusion constant D_B = 7.3 $\mu m^2/s$ was used to generate the theoretical curves in Fig. 9 E. An F test was used to assess goodness of fit of the modeled curves to the observed results. Note that the standard deviation for D_B of 2.8 $\mu m^2/s$ also includes error in S_0 and B_0 (the latter caused by uncertainty in reported values for cilium geometry; Gilliam et al., 2012). From D_B = 7.3 $\mu m^2/s$, we find that t^* = 33 s for $[B]_0$ = 27.5 nM; t^* = 8 s for $[B]_0$ = 110 nM; $\hat{t}$ = 3 h for $[B]_0$ = 27.5 nM; and $\hat{t}$ = 11 min for $[B]_0$ = 110 nM.

Online supplemental material

Fig. S1 shows additional validation of the semipermeabilized cell assay. Fig. S2 shows filipin staining and TIRF imaging of IMCD3 cell cilia. Fig. S3 shows size-dependent cilia entry of GBP fusion proteins and size-independent access of these proteins as well as large FKBP fusions to the plasma membrane. Fig. S4 shows kinetics of MBP-GBP cilia entry in WGA-treated cells relative to untreated cells as well as weak accumulation of GFP alone near the cilium base. Fig. S5 provides further evidence that WGA cross-links and immobilizes Sstr3-GFP and shows absolute quantification of Sstr3-GFP concentration in cilia by comparison to viral particles bearing exactly 120 GFP molecules. Video 1 shows kinetics of GBP, Trx-GBP, and MBP-GBP capture in cilia of digitonin-permeabilized cells. Online supplemental material is available at http://www.jcb.org/cgi/content/full/jcb.201212024/DC1.

We thank A. Straight and W.J. Nelson for generously sharing microscopes, J. Liang for help with video editing and development of the in vivo assay for diffusion into cilia, and A. Amodeo for preparation of the *Xenopus* egg extract. We thank M. Bornens, T. Caspary, K.C. Garcia, D. Görlich, S. Munro, M. Hetzer, A. Johnson, T. Meyer, K. Mykytyn, and R. Tsien for sharing antibodies and plasmids, P. Miller for help with initial characterization of GBPs, H. Jin for generating the GFP-IFT88 cell line, C. Fuller and F. Ye for assistance with live imaging, and members of the Nachury laboratory for helpful discussions.

This work was supported by grants to M.V. Nachury from the National Institutes of Health (GM089933) and the March of Dimes (1-FY11-517) and by the Connie and Bob Lurie Fellowship of the Damon Runyon Cancer Research Foundation to D.K. Breslow (DRG 2087-11).

Submitted: 6 December 2012
Accepted: 11 July 2013

References

Adam, S.A., R.S. Marr, and L. Gerace. 1990. Nuclear protein import in permeabilized mammalian cells requires soluble cytoplasmic factors. *J. Cell Biol.* 111:807–816. http://dx.doi.org/10.1083/jcb.111.3.807

Besschetnova, T.Y., B. Roy, and J.V. Shah. 2009. Imaging intraflagellar transport in mammalian primary cilia. *Methods Cell Biol.* 93:331–346. http://dx.doi.org/10.1016/S0091-679X(08)93016-8

Calvert, P.D., V.I. Govardovskii, N. Krasnoperova, R.E. Anderson, J. Lem, and C.L. Makino. 2001. Membrane protein diffusion sets the speed of rod phototransduction. *Nature*. 411:90–94. http://dx.doi.org/10.1038/35075083

Calvert, P.D., W.E. Schiesser, and E.N. Pugh Jr. 2010. Diffusion of a soluble protein, photoactivatable GFP, through a sensory cilium. *J. Gen. Physiol.* 135:173–196. http://dx.doi.org/10.1085/jgp.200910322

Charpilienne, A., M. Nejmeddine, M. Berois, N. Parez, E. Neumann, E. Hewat, G. Trugnan, and J. Cohen. 2001. Individual rotavirus-like particles containing 120 molecules of fluorescent protein are visible in living cells. *J. Biol. Chem.* 276:29361–29367. http://dx.doi.org/10.1074/jbc.M101935200

Chih, B., P. Liu, Y. Chinn, C. Chalouni, L.G. Komuves, P.E. Hass, W. Sandoval, and A.S. Peterson. 2012. A ciliopathy complex at the transition zone protects the cilia as a privileged membrane domain. *Nat. Cell Biol.* 14:61–72. http://dx.doi.org/10.1038/ncb2410

Chung, I., R. Akita, R. Vandlen, D. Toomre, J. Schlessinger, and I. Mellman. 2010. Spatial control of EGF receptor activation by reversible dimerization on living cells. *Nature*. 464:783–787. http://dx.doi.org/10.1038/nature08827

Crank, J. 2001. The Mathematics of Diffusion. Oxford University Press, Oxford, England, UK. 414 pp.

Czajkowsky, D.M., E.M. Hotze, Z. Shao, and R.K. Tweten. 2004. Vertical collapse of a cytolysin prepore moves its transmembrane beta-hairpins to the membrane. *EMBO J.* 23:3206–3215. http://dx.doi.org/10.1038/sj.emboj.7600350

Davis, L.I., and G. Blobel. 1986. Identification and characterization of a nuclear pore complex protein. *Cell*. 45:699–709. http://dx.doi.org/10.1016/0092-8674(86)90784-1

Davis, L.I., and G. Blobel. 1987. Nuclear pore complex contains a family of glycoproteins that includes p62: glycosylation through a previously unidentified cellular pathway. *Proc. Natl. Acad. Sci. USA*. 84:7552–7556. http://dx.doi.org/10.1073/pnas.84.21.7552

Dishinger, J.F., H.L. Kee, P.M. Jenkins, S. Fan, T.W. Hurd, J.W. Hammond, Y.N.-T. Truong, B. Margolis, J.R. Martens, and K.J. Verhey. 2010. Ciliary entry of the kinesin-2 motor KIF17 is regulated by importin-beta2 and RanGTP. *Nat. Cell Biol.* 12:703–710. http://dx.doi.org/10.1038/ncb2073

Dix, J.A., and A.S. Verkman. 2008. Crowding effects on diffusion in solutions and cells. *Annu Rev Biophys*. 37:247–263. http://dx.doi.org/10.1146/annurev.biophys.37.032807.125824

Elowitz, M.B., M.G. Surette, P.E. Wolf, J.B. Stock, and S. Leibler. 1999. Protein mobility in the cytoplasm of *Escherichia coli*. *J. Bacteriol.* 181:197–203.

Emig, S., D. Schmalz, M. Shakibaei, and K. Buchner. 1995. The nuclear pore complex protein p62 is one of several sialic acid-containing proteins of the nuclear envelope. *J. Biol. Chem.* 270:13787–13793. http://dx.doi.org/10.1074/jbc.270.23.13787

Engel, B.D., H. Ishikawa, K.A. Wemmer, S. Geimer, K.-I. Wakabayashi, M. Hirono, B. Craige, G.J. Pazour, G.B. Witman, R. Kamiya, and W.F. Marshall. 2012. The role of retrograde intraflagellar transport in flagellar assembly, maintenance, and function. *J. Cell Biol.* 199:151–167. http://dx.doi.org/10.1083/jcb.201206068

Fan, S., E.L. Whiteman, T.W. Hurd, J.C. McIntyre, J.F. Dishinger, C.J. Liu, J.R. Martens, K.J. Verhey, U. Sajjan, and B.L. Margolis. 2011. Induction of Ran GTP drives ciliogenesis. *Mol. Biol. Cell*. 22:4539–4548. http://dx.doi.org/10.1091/mbc.E11-03-0267

Finlay, D.R., D.D. Newmeyer, T.M. Price, and D.J. Forbes. 1987. Inhibition of in vitro nuclear transport by a lectin that binds to nuclear pores. *J. Cell Biol.* 104:189–200. http://dx.doi.org/10.1083/jcb.104.2.189

Flanagan, J.J., R.K. Tweten, A.E. Johnson, and A.P. Heuck. 2009. Cholesterol exposure at the membrane surface is necessary and sufficient to trigger perfringolysin O binding. *Biochemistry*. 48:3977–3987. http://dx.doi.org/10.1021/bi9002309

Follit, J.A., R.A. Tuft, K.E. Fogarty, and G.J. Pazour. 2006. The intraflagellar transport protein IFT20 is associated with the Golgi complex and is required for cilia assembly. *Mol. Biol. Cell*. 17:3781–3792. http://dx.doi.org/10.1091/mbc.E06-02-0133

Follit, J.A., L. Li, Y. Vucica, and G.J. Pazour. 2010. The cytoplasmic tail of fibrocystin contains a ciliary targeting sequence. *J. Cell Biol.* 188:21–28. http://dx.doi.org/10.1083/jcb.200910096

Francis, S.S., J. Sfakianos, B. Lo, and I. Mellman. 2011. A hierarchy of signals regulates entry of membrane proteins into the ciliary membrane domain in epithelial cells. *J. Cell Biol.* 193:219–233. http://dx.doi.org/10.1083/jcb.201009001

Gilliam, J.C., J.T. Chang, I.M. Sandoval, Y. Zhang, T. Li, S.J. Pittler, W. Chiu, and T.G. Wensel. 2012. Three-dimensional architecture of the rod sensory cilium and its disruption in retinal neurodegeneration. *Cell*. 151:1029–1041. http://dx.doi.org/10.1016/j.cell.2012.10.038

Gillingham, A.K., and S. Munro. 2000. The PACT domain, a conserved centrosomal targeting motif in the coiled-coil proteins AKAP450 and pericentrin. *EMBO Rep.* 1:524–529.

Goetz, S.C., and K.V. Anderson. 2010. The primary cilium: a signalling centre during vertebrate development. *Nat. Rev. Genet.* 11:331–344. http://dx.doi.org/10.1038/nrg2774

Golan, D.E., C.S. Brown, C.M. Cianci, S.T. Furlong, and J.P. Caulfield. 1986. Schistosomula of *Schistosoma mansoni* use lysophosphatidylcholine to lyse adherent human red blood cells and immobilize red cell membrane components. *J. Cell Biol.* 103:819–828. http://dx.doi.org/10.1083/jcb.103.3.819

Händel, M., S. Schulz, A. Stanarius, M. Schreff, M. Erdtmann-Vourliotis, H. Schmidt, G. Wolf, and V. Höllt. 1999. Selective targeting of somatostatin receptor 3 to neuronal cilia. *Neuroscience*. 89:909–926. http://dx.doi.org/10.1016/S0306-4522(98)00354-6

Hao, L., M. Thein, I. Brust-Mascher, G. Civelekoglu-Scholey, Y. Lu, S. Acar, B. Prevo, S. Shaham, and J.M. Scholey. 2011. Intraflagellar transport delivers tubulin isotypes to sensory cilium middle and distal segments. *Nat. Cell Biol.* 13:790–798. http://dx.doi.org/10.1038/ncb2268

Harbury, P.B., T. Zhang, P.S. Kim, and T. Alber. 1993. A switch between two-, three-, and four-stranded coiled coils in GCN4 leucine zipper mutants. *Science*. 262:1401–1407. http://dx.doi.org/10.1126/science.8248779

Heuck, A.P., P.C. Moe, and B.B. Johnson. 2010. The cholesterol-dependent cytolysin family of gram-positive bacterial toxins. *Subcell. Biochem.* 51:551–577. http://dx.doi.org/10.1007/978-90-481-8622-8_20

Hoelz, A., E.W. Debler, and G. Blobel. 2011. The structure of the nuclear pore complex. *Annu. Rev. Biochem.* 80:613–643. http://dx.doi.org/10.1146/annurev-biochem-060109-151030

Hu, Q., L. Milenkovic, H. Jin, M.P. Scott, M.V. Nachury, E.T. Spiliotis, and W.J. Nelson. 2010. A septin diffusion barrier at the base of the primary cilium maintains ciliary membrane protein distribution. *Science*. 329:436–439. http://dx.doi.org/10.1126/science.1191054

Ishikawa, H., and W.F. Marshall. 2011. Ciliogenesis: building the cell's antenna. *Nat. Rev. Mol. Cell Biol.* 12:222–234. http://dx.doi.org/10.1038/nrm3085

Jaqaman, K., H. Kuwata, N. Touret, R. Collins, W.S. Trimble, G. Danuser, and S. Grinstein. 2011. Cytoskeletal control of CD36 diffusion promotes its receptor and signaling function. *Cell*. 146:593–606. http://dx.doi.org/10.1016/j.cell.2011.06.049

Jin, H., S.R. White, T. Shida, S. Schulz, M. Aguiar, S.P. Gygi, J.F. Bazan, and M.V. Nachury. 2010. The conserved Bardet-Biedl syndrome proteins assemble a coat that traffics membrane proteins to cilia. *Cell*. 141:1208–1219. http://dx.doi.org/10.1016/j.cell.2010.05.015

Joglekar, A.P., E.D. Salmon, and K.S. Bloom. 2008. Counting kinetochore protein numbers in budding yeast using genetically encoded fluorescent proteins. *Methods Cell Biol.* 85:127–151. http://dx.doi.org/10.1016/S0091-679X(08)85007-8

Kee, H.L., J.F. Dishinger, T.L. Blasius, C.-J. Liu, B. Margolis, and K.J. Verhey. 2012. A size-exclusion permeability barrier and nucleoporins characterize a ciliary pore complex that regulates transport into cilia. *Nat. Cell Biol.* 14:431–437. http://dx.doi.org/10.1038/ncb2450

Kirchhofer, A., J. Helma, K. Schmidthals, C. Frauer, S. Cui, A. Karcher, M. Pellis, S. Muyldermans, C.S. Casas-Delucchi, M.C. Cardoso, et al. 2010. Modulation of protein properties in living cells using nanobodies. *Nat. Struct. Mol. Biol.* 17:133–138. http://dx.doi.org/10.1038/nsmb.1727

Knibbs, R.N., I.J. Goldstein, R.M. Ratcliffe, and N. Shibuya. 1991. Characterization of the carbohydrate binding specificity of the leukoagglutinating lectin from *Maackia amurensis*. Comparison with other sialic acid-specific lectins. *J. Biol. Chem.* 266:83–88.

Komatsu, T., I. Kukelyansky, J.M. McCaffery, T. Ueno, L.C. Varela, and T. Inoue. 2010. Organelle-specific, rapid induction of molecular activities and membrane tethering. *Nat. Methods*. 7:206–208. http://dx.doi.org/10.1038/nmeth.1428

Kutay, U., E. Izaurralde, F.R. Bischoff, I.W. Mattaj, and D. Görlich. 1997. Dominant-negative mutants of importin-beta block multiple pathways of import and export through the nuclear pore complex. *EMBO J.* 16:1153–1163. http://dx.doi.org/10.1093/emboj/16.6.1153

Lin, Y.C., P. Niewiadomski, B. Lin, H. Nakamura, S.C. Phua, J. Jiao, A. Levchenko, T. Inoue, R. Rohatgi, and T. Inoue. 2013. Chemically inducible diffusion trap at cilia reveals molecular sieve-like barrier. *Nat. Chem. Biol.* 9:437–443. http://dx.doi.org/10.1038/nchembio.1252

Luby-Phelps, K. 2000. Cytoarchitecture and physical properties of cytoplasm: volume, viscosity, diffusion, intracellular surface area. *Int. Rev. Cytol.* 192:189–221. http://dx.doi.org/10.1016/S0074-7696(08)60527-6

Marshall, W.F., H. Qin, M. Rodrigo Brenni, and J.L. Rosenbaum. 2005. Flagellar length control system: testing a simple model based on intraflagellar transport and turnover. *Mol. Biol. Cell*. 16:270–278. http://dx.doi.org/10.1091/mbc.E04-07-0586

Marshallsay, C., and R. Lührmann. 1994. In vitro nuclear import of snRNPs: cytosolic factors mediate m3G-cap dependence of U1 and U2 snRNP transport. *EMBO J.* 13:222–231.

Michaud, N., and D. Goldfarb. 1992. Microinjected U snRNAs are imported to oocyte nuclei via the nuclear pore complex by three distinguishable targeting pathways. *J. Cell Biol.* 116:851–861. http://dx.doi.org/10.1083/jcb.116.4.851

Mohr, D., S. Frey, T. Fischer, T. Güttler, and D. Görlich. 2009. Characterisation of the passive permeability barrier of nuclear pore complexes. *EMBO J.* 28:2541–2553. http://dx.doi.org/10.1038/emboj.2009.200

Moree, B., C.B. Meyer, C.J. Fuller, and A.F. Straight. 2011. CENP-C recruits M18BP1 to centromeres to promote CENP-A chromatin assembly. *J. Cell Biol.* 194:855–871. http://dx.doi.org/10.1083/jcb.201106079

Nachury, M.V., E.S. Seeley, and H. Jin. 2010. Trafficking to the ciliary membrane: how to get across the periciliary diffusion barrier? *Annu. Rev. Cell Dev. Biol.* 26:59–87. http://dx.doi.org/10.1146/annurev.cellbio.042308.113337

Nagata, Y., and M.M. Burger. 1974. Wheat germ agglutinin. Molecular characteristics and specificity for sugar binding. *J. Biol. Chem.* 249:3116–3122.

Nair, K.S., S.M. Hanson, A. Mendez, E.V. Gurevich, M.J. Kennedy, V.I. Shestopalov, S.A. Vishnivetskiy, J. Chen, J.B. Hurley, V.V. Gurevich, and V.Z. Slepak. 2005. Light-dependent redistribution of arrestin in vertebrate rods is an energy-independent process governed by protein-protein interactions. *Neuron*. 46:555–567. http://dx.doi.org/10.1016/j.neuron.2005.03.023

Najafi, M., and P.D. Calvert. 2012. Transport and localization of signaling proteins in ciliated cells. *Vision Res.* 75:11–18. http://dx.doi.org/10.1016/j.visres.2012.08.006

Najafi, M., N.A. Maza, and P.D. Calvert. 2012. Steric volume exclusion sets soluble protein concentrations in photoreceptor sensory cilia. *Proc. Natl. Acad. Sci. USA*. 109:203–208. http://dx.doi.org/10.1073/pnas.1115109109

Nakada, C., K. Ritchie, Y. Oba, M. Nakamura, Y. Hotta, R. Iino, R.S. Kasai, K. Yamaguchi, T. Fujiwara, and A. Kusumi. 2003. Accumulation of anchored proteins forms membrane diffusion barriers during neuronal polarization. *Nat. Cell Biol.* 5:626–632. http://dx.doi.org/10.1038/ncb1009

Nehring, R.B., D. Richter, and W. Meyerhof. 2000. Glycosylation affects agonist binding and signal transduction of the rat somatostatin receptor subtype 3. *J. Physiol. Paris*. 94:185–192. http://dx.doi.org/10.1016/S0928-4257(00)00203-5

Nilsson, B., T. Moks, B. Jansson, L. Abrahmsén, A. Elmblad, E. Holmgren, C. Henrichson, T.A. Jones, and M. Uhlén. 1987. A synthetic IgG-binding domain based on staphylococcal protein A. *Protein Eng.* 1:107–113. http://dx.doi.org/10.1093/protein/1.2.107

Ocbina, P.J., J.T. Eggenschwiler, I. Moskowitz, and K.V. Anderson. 2011. Complex interactions between genes controlling trafficking in primary cilia. *Nat. Genet.* 43:547–553. http://dx.doi.org/10.1038/ng.832

Olofsson, A., H. Hebert, and M. Thelestam. 1993. The projection structure of perfringolysin O (*Clostridium perfringens* theta-toxin). *FEBS Lett.* 319:125–127. http://dx.doi.org/10.1016/0014-5793(93)80050-5

Pedersen, L.B., and J.L. Rosenbaum. 2008. Intraflagellar transport (IFT) role in ciliary assembly, resorption and signalling. *Curr. Top. Dev. Biol.* 85:23–61. http://dx.doi.org/10.1016/S0070-2153(08)00802-8

Reiter, J.F., O.E. Blacque, and M.R. Leroux. 2012. The base of the cilium: roles for transition fibres and the transition zone in ciliary formation, maintenance and compartmentalization. *EMBO Rep.* 13:608–618. http://dx.doi.org/10.1038/embor.2012.73

Ribbeck, K., and D. Görlich. 2002. The permeability barrier of nuclear pore complexes appears to operate via hydrophobic exclusion. *EMBO J.* 21:2664–2671. http://dx.doi.org/10.1093/emboj/21.11.2664

Rosenzweig, D.H., K.S. Nair, J. Wei, Q. Wang, G. Garwin, J.C. Saari, C.-K. Chen, A.V. Smrcka, A. Swaroop, J. Lem, et al. 2007. Subunit dissociation and diffusion determine the subcellular localization of rod and cone transducins. *J. Neurosci.* 27:5484–5494. http://dx.doi.org/10.1523/JNEUROSCI.1421-07.2007

Schulz, I. 1990. Permeabilizing cells: some methods and applications for the study of intracellular processes. *Methods Enzymol.* 192:280–300. http://dx.doi.org/10.1016/0076-6879(90)92077-Q

Sharma, N., Z.A. Kosan, J.E. Stallworth, N.F. Berbari, and B.K. Yoder. 2011. Soluble levels of cytosolic tubulin regulate ciliary length control. *Mol. Biol. Cell.* 22:806–816. http://dx.doi.org/10.1091/mbc.E10-03-0269

Shepard, L.A., A.P. Heuck, B.D. Hamman, J. Rossjohn, M.W. Parker, K.R. Ryan, A.E. Johnson, and R.K. Tweten. 1998. Identification of a membrane-spanning domain of the thiol-activated pore-forming toxin *Clostridium perfringens* perfringolysin O: an alpha-helical to beta-sheet transition identified by fluorescence spectroscopy. *Biochemistry*. 37:14563–14574. http://dx.doi.org/10.1021/bi981452f

Song, A.-H., D. Wang, G. Chen, Y. Li, J. Luo, S. Duan, and M.-M. Poo. 2009. A selective filter for cytoplasmic transport at the axon initial segment. *Cell*. 136:1148–1160. http://dx.doi.org/10.1016/j.cell.2009.01.016

Suzuki, K., K. Ritchie, E. Kajikawa, T. Fujiwara, and A. Kusumi. 2005. Rapid hop diffusion of a G-protein-coupled receptor in the plasma membrane as revealed by single-molecule techniques. *Biophys. J.* 88:3659–3680. http://dx.doi.org/10.1529/biophysj.104.048538

Takao, D., and S. Kamimura. 2008. FRAP analysis of molecular diffusion inside sea-urchin spermatozoa. *J. Exp. Biol.* 211:3594–3600. http://dx.doi.org/10.1242/jeb.021923

Tran, P.V., C.J. Haycraft, T.Y. Besschetnova, A. Turbe-Doan, R.W. Stottmann, B.J. Herron, A.L. Chesebro, H. Qiu, P.J. Scherz, J.V. Shah, et al. 2008. THM1 negatively modulates mouse sonic hedgehog signal transduction and affects retrograde intraflagellar transport in cilia. *Nat. Genet.* 40:403–410. http://dx.doi.org/10.1038/ng.105

Wang, Q., J. Pan, and W.J. Snell. 2006. Intraflagellar transport particles participate directly in cilium-generated signaling in *Chlamydomonas*. *Cell*. 125:549–562. http://dx.doi.org/10.1016/j.cell.2006.02.044

Winckler, B., P. Forscher, and I. Mellman. 1999. A diffusion barrier maintains distribution of membrane proteins in polarized neurons. *Nature*. 397:698–701. http://dx.doi.org/10.1038/17806

Ye, F., D.K. Breslow, E.F. Koslover, A.J. Spakowitz, W.J. Nelson, and M.V. Nachury. 2013. Single molecule imaging reveals a major role for diffusion in the exploration of ciliary space by signaling receptors. *eLife*. 2:e00654. http://dx.doi.org/10.7554/eLife.00654